Revisiting the structure, age, and evolution of the Wharton Basin to better understand subduction under Indonesia

Jensen Jacob, Jérôme Dyment, V Yatheesh

JOURNAL OF GEOPHYSICAL RESEARCH: SOLID EARTH, VOL. 119, 169–190, doi:10.1002/2013JB010285, 2014

Revisiting the structure, age, and evolution of the Wharton Basin to better understand subduction under Indonesia

Jensen Jacob,[1] Jérôme Dyment,[1] and V. Yatheesh[2]

Received 15 April 2013; revised 25 November 2013; accepted 26 November 2013; published 31 January 2014.

[1] Understanding the subduction processes along the Sunda Trench requires detailed constraints on the subducting lithosphere. We build a detailed tectonic map of the Wharton Basin based on reinterpretation of satellite-derived gravity anomalies and marine magnetic anomalies. The Wharton Basin is characterized by a fossil ridge, dated ~36.5 Ma, offset by N-S fracture zones. Magnetic anomalies 18 to 34 (38–84 Ma) are identified on both flanks, although a large part of the basin has been subducted. We analyze the past plate kinematic evolution of the Wharton Basin by two-plate (India-Australia) and three-plate (India-Australia-Antarctica) reconstructions. Despite the diffuse plate boundaries within the Indo-Australian plate for the last 20 Ma, we obtain finite rotation parameters that we apply to reconstruct the subducted Wharton Basin and constrain the thickness, buoyancy, and rheology of the subducting plate. The lower subductability of younger lithosphere off Sumatra has important consequences on the morphology, with a shallower trench, forearc islands, and a significant inward deviation of the subduction system. This deviation decreases in the youngest area, where the Wharton fossil spreading center enters subduction: The discontinuous magmatic crust and serpentinized upper mantle, consequences of the slow spreading rates at which this area was formed, weaken the mechanical resistance to subduction and facilitate the restoration of the accretionary prism. Deeper effects include the possible creation of asthenospheric windows beneath the Andaman Sea, in relation to the long-offset fracture zones, and east of 105°E, as a result of subduction of the spreading center.

Citation: Jacob, J., J. Dyment, and V. Yatheesh (2014), Revisiting the structure, age, and evolution of the Wharton Basin to better understand subduction under Indonesia, *J. Geophys. Res. Solid Earth*, *119*, 169–190, doi:10.1002/2013JB010285.

1. Introduction

[2] The disastrous earthquake and tsunami of 26 December 2004 in northern Sumatra, and some subsequent important earthquakes in central and southern Sumatra (28 March 2005; 12 September 2007, to cite only the recent ones with magnitude higher than 8) and in the oceanic plate off Sumatra (11 April 2012) have triggered a number of investigations to better understand the generation and mechanism of these earthquakes and the subduction process. An important constraint for such an understanding is the nature, geometry, and physical properties of the oceanic lithosphere involved in the subduction, which in turns depends on its age and tectonic evolution. The oceanic basin subducting along the Sunda Trench under Sumatra belongs to the Wharton Basin (Figure 1). In this paper we reexamine this basin to (1) depict its age, structure, and tectonic evolution from a detailed identification of magnetic lineations and fracture zones of the basin; (2) reconstruct the age and structure of the missing part of the basin subducted beneath the Sunda Trench and make inferences on its geometry and physical properties; and (3) examine the possible consequences on subduction at the Sunda Trench. Apart from this, the present investigation also provides the opportunity to revisit the plate kinematics of the whole Eastern Indian Ocean between 84 and 45 Ma and brings new constraints on the controversial motion of Australia and Antarctica in the initial stages of their separation.

[3] The Eastern Indian Ocean results from the breakup, opening, and seafloor spreading between the Indian, Australian, and Antarctic plates. India separated from Antarctica and Australia at about 130 Ma, forming the Enderby Basin off Antarctica and the Bay of Bengal off India (between India and Antarctica [*Ramana et al*., 2001; *Gaina et al*., 2007]), and the Perth, Cuvier, and Gascoyne basins off Australia (between India and Australia [e.g., *Gibbons et al*., 2012]). A major plate reorganization occurred at about 100 Ma, resulting in a ~40° clockwise reorientation of the spreading direction, forming the Crozet Basin and the eastern part of the Central Indian Basin between India and Antarctica on one hand, the Wharton Basin between India and Australia on the other hand. At the same time, seafloor spreading started at a very slow rate between Australia and Antarctica, forming the Australian-Antarctic Basin [e.g., *Johnson et al*., 1976]. The first contact of the Indian continent with arcs belonging to the Eurasian continent ("soft collision") might have occurred at Chron 22

[1]Institut de Physique du Globe de Paris and CNRS, Sorbonne Paris Cité, Paris, France.
[2]CSIR-National Institute of Oceanography, Dona Paula, Goa, India.

Corresponding author: J. Dyment, Institut de Physique du Globe de Paris, 1 rue Jussieu, FR-75238 Paris CEDEX 05, France. (jdy@ipgp.fr)

2169-9313/14/10.1002/2013JB010285

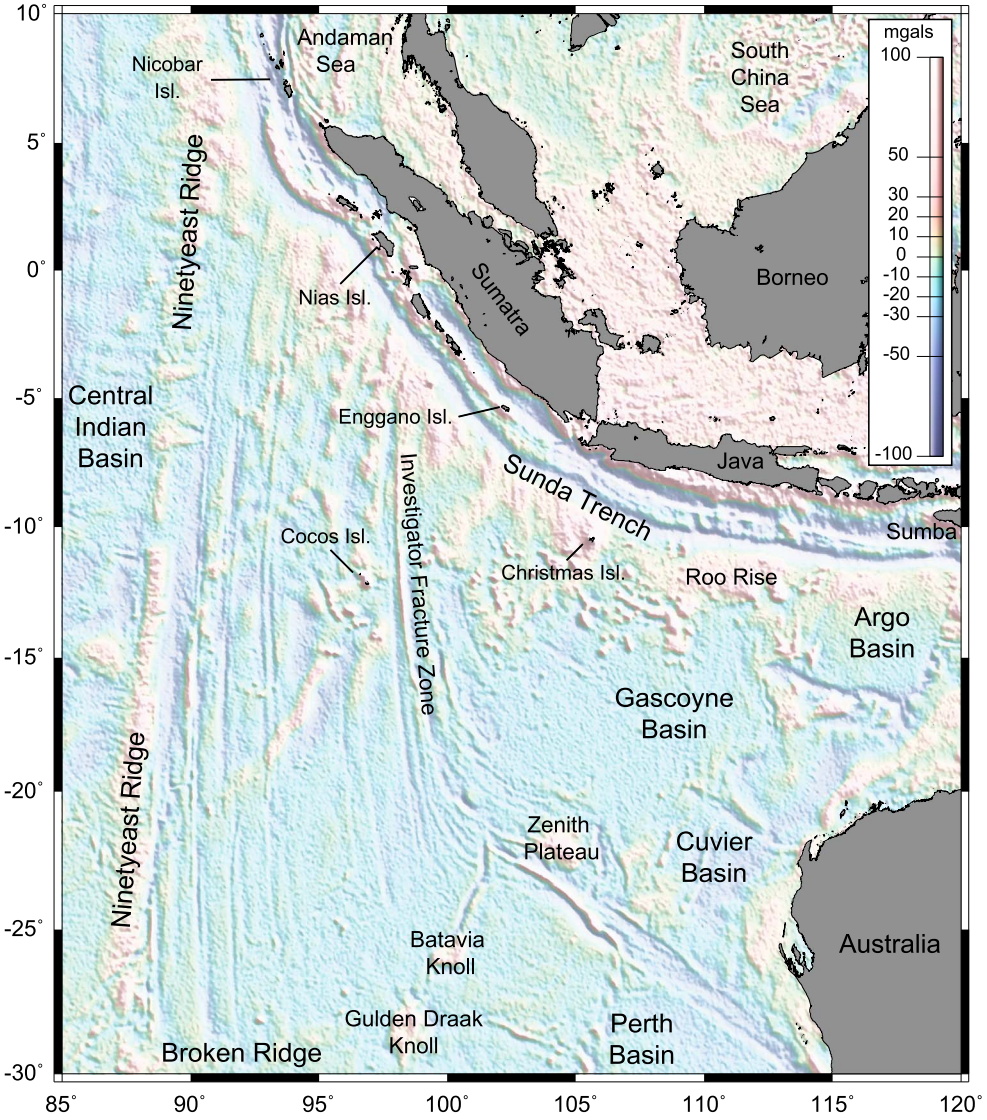

Figure 1. Free-air gravity anomaly map derived from satellite altimetry [*Sandwell and Smith*, 2009] over the Wharton Basin area. Also shown is the location of the geographic, bathymetric, and structural features discussed in the paper.

(49.4 Ma; Table 1), resulting in a sharp slowdown of the northward drift of India, whereas the "hard collision" took place between Chrons 20 and 18 (~40 Ma), leading to a ~50° clockwise change of the spreading direction between India and Antarctica [*Patriat and Achache*, 1984]. Seafloor spreading along the Wharton ridge ceased at this time, as shown by the presence of a fossil spreading center in the Wharton Basin [*Liu et al*., 1983]. After this episode, the Indian and Australian plates became attached to form a single "Indo-Australian" plate and spreading accelerated suddenly between Australia and Antarctica, a plate boundary that became the eastern section of the Southeast Indian Ridge.

[4] Previous interpretations of the marine magnetic anomalies in the Wharton Basin have progressively unraveled this history, from the initial identification of the anomalies [*Sclater and Fisher*, 1974] to the recognition of the fossil spreading center [*Liu et al*., 1983] and subsequent plate tectonic models for the evolution of the basin [*Royer et al*., 1991; *Krishna et al*., 1995]. Here we reinvestigate the Wharton Basin using an updated compilation of magnetic anomaly data and taking advantage of the analytic signal technique to determine objectively the location of the magnetic isochrons.

2. Data and Methods

[5] The main data used for the present study are the sea surface magnetic profiles obtained from the Geophy-sical Data System database (National Geophysical Data Centre, Boulder, Colorado). Additional data have been obtained through the US-French project "Indian Ocean Data Compilation Project" (1986–1990) [*Sclater et al*., 1997]. Magnetic data acquired during French cruises SAMUDRA of R/V *L'Atalante* (Deplus, personal communication, 2008), DEFLO (Patriat, personal communication, 2009), ANDAMAN (Chamot-Rooke, personal communication, 2008) and SUMATRA-OBS (Singh, personal communication, 2009) of R/V *Marion Dufresne*, and some Indo-Russian profiles collected during the Tran-

Table 1. Age of Magnetic Anomalies According to Two Geomagnetic Polarity Timescales (G2004: After *Gradstein et al.* [2004] and CK1995: After *Cande and Kent* [1995])

Chron	Age (G2004)	Age (CK1995)
15o	35.043	34.940
17y	36.512	36.618
18y	38.032	38.426
18o	39.464	40.130
20y	41.590	42.536
20o	42.774	43.789
21y	45.346	46.264
21o	47.235	47.906
22y	48.599	49.037
22o	49.427	49.714
23y	50.730	50.778
23o	51.901	51.743
24y	52.648	52.364
24o	53.808	53.347
25y	56.665	55.904
25o	57.180	56.391
26y	58.379	57.554
26o	58.737	57.911
27y	61.650	60.920
27o	61.983	61.276
28y	63.104	62.499
28o	64.128	63.634
29y	64.432	63.976
29o	65.118	64.745
30y	65.861	65.578
30o	67.696	67.610
31o	68.732	68.737
32y	70.961	71.071
32o	72.929	73.004
33y	73.577	73.619
33o	79.543	79.075
34y	84.000	83.000
M0	124.600	
M11	135.500	

Indian Ocean Geotraverse Program (Krishna, personal communication, 2008) are also included. As a preliminary step the whole data set has been corrected for navigational errors and spikes. The International Geomagnetic Reference Field [International Association of Geomagnetism and Aeronomy, Working Group(*IAGA WG) V-MOD*, 2010] has been removed from the total field data to obtain a magnetic anomaly data set.

[6] The free air gravity anomaly and "predicted" bathymetry maps, both derived from satellite altimetry data [*Smith and Sandwell*, 1997; *Sandwell and Smith*, 2009] help to identify and locate fracture zones, fossil spreading axes, oceanic plateaus, aseismic ridges, seamounts, and the subduction zone. They are locally complemented by multibeam bathymetry of cruises SAMUDRA [*Deplus et al*., 1998], ANDAMAN (Chamot-Rooke, personal communication, 2008) and SUMATRA OBS (Singh, personal communication, 2009), as well as several published maps [e.g., *Ladage et al*., 2006; *Kopp et al*., 2008; *Graindorge et al*., 2008].

[7] Different techniques are used to identify the magnetic anomalies and locate the isochrons in the Wharton Basin. In the first stage we apply the conventional method of interprofile correlation and the comparison with synthetic anomaly models. Characteristic tiny wiggles [*Cande and Kent*, 1992] are also considered to identify unambiguously some of the magnetic anomalies [e.g., *Dyment*, 1998]. The analytic signal is used in a second stage to demarcate objectively the boundaries of the magnetized blocks. In this study, we follow *Cande et al*. [2010] and use consistently the geomagnetic polarity timescale (GPTS) of *Gradstein et al*. [2004] (Table 1), although the GPTS of *Cande and Kent* [1995] (Table 1) is also used to estimate the uncertainty in spreading rate calculations (section 4.3).

[8] The shape of a magnetic anomaly is influenced by the geometry of a magnetized body, the strength and orientation of the magnetization vector, and the orientation of the present magnetic field. Under the assumption of a dipolar paleomagnetic field, the orientation of the magnetization vector only depends on the latitude at the time of acquisition of the magnetization. As a result of the nonvertical orientation of the past and present magnetic field, magnetic anomalies do not simply relate to their causative source bodies but exhibit a complicated shape made of two or three positive and negative lobes. On profiles, it translates to a phase shift, also known as "skewness" [e.g., *Schouten and McCamy*, 1972; *Cande*, 1976; *Dyment et al*., 1994]. Correcting for this skewness requires not only the knowledge of the present day field (the International Geomagnetic Reference Field) but also the paleolatitude and paleo-azimuth, i.e., the plate rotation with respect to the geomagnetic field since the acquisition of magnetization. These parameters are, however, poorly constrained. Moreover, an additional skewness, the "anomalous skewness", is also observed and reflects more complicated field evolution and/or shape of the source body [*Cande*, 1976; *Dyment and Arkani-Hamed*, 1995]. As a better way to avoid the effect of skewness on the magnetic anomaly signal, we compute the modulus of the analytic signal [*Nabighian*, 1972, 1974; *Roest et al*., 1992]. The resultant signal is a zero phase signal which represents an envelope of all the possible phase shifts of the observed magnetic anomaly and has maximum amplitude at the place where the magnetic polarity contrast is maximal. The analytic signal method is therefore useful to detect the location of vertical boundaries between blocks of opposite magnetic polarity on the oceanic crust [e.g., *Chaubey et al*., 2002]. This method is efficient, reliable, and much more objective than the conventional method of picking by visual comparison of observed and synthetic anomaly models. The latter is, however, essential to identify the sequences of anomalies and ascribe an age to the picks.

3. Fracture Zones, Magnetic Lineations, and the Evolution of the Wharton Basin

[9] The Wharton Basin is dissected by a series of north–south trending continuous fracture zones, which divide it into eight compartments A to H (Figure 2). We have only numbered the compartments in which magnetic anomalies have been identified, i.e., the main compartments and the narrow compartment D. Some very narrow (< 40 km) segments exist between double or multiple fracture zones. The fracture zones are subparallel to the Ninetyeast Ridge, a prominent volcanic structure bounding the Wharton Basin to the west. In detail, the Ninetyeast Ridge is actually bounded by two fracture zones: in the north, by the Ninetyeast Fracture Zone [*Royer et al*., 1991] that bounds compartment B to the west, and in the south by the 88.5°E Fracture Zone [*Royer and Sandwell*, 1989] that bounds compartment A to the west. The magmatism that created the Ninetyeast Ridge seems to be channeled by the preexisting fracture zones of the

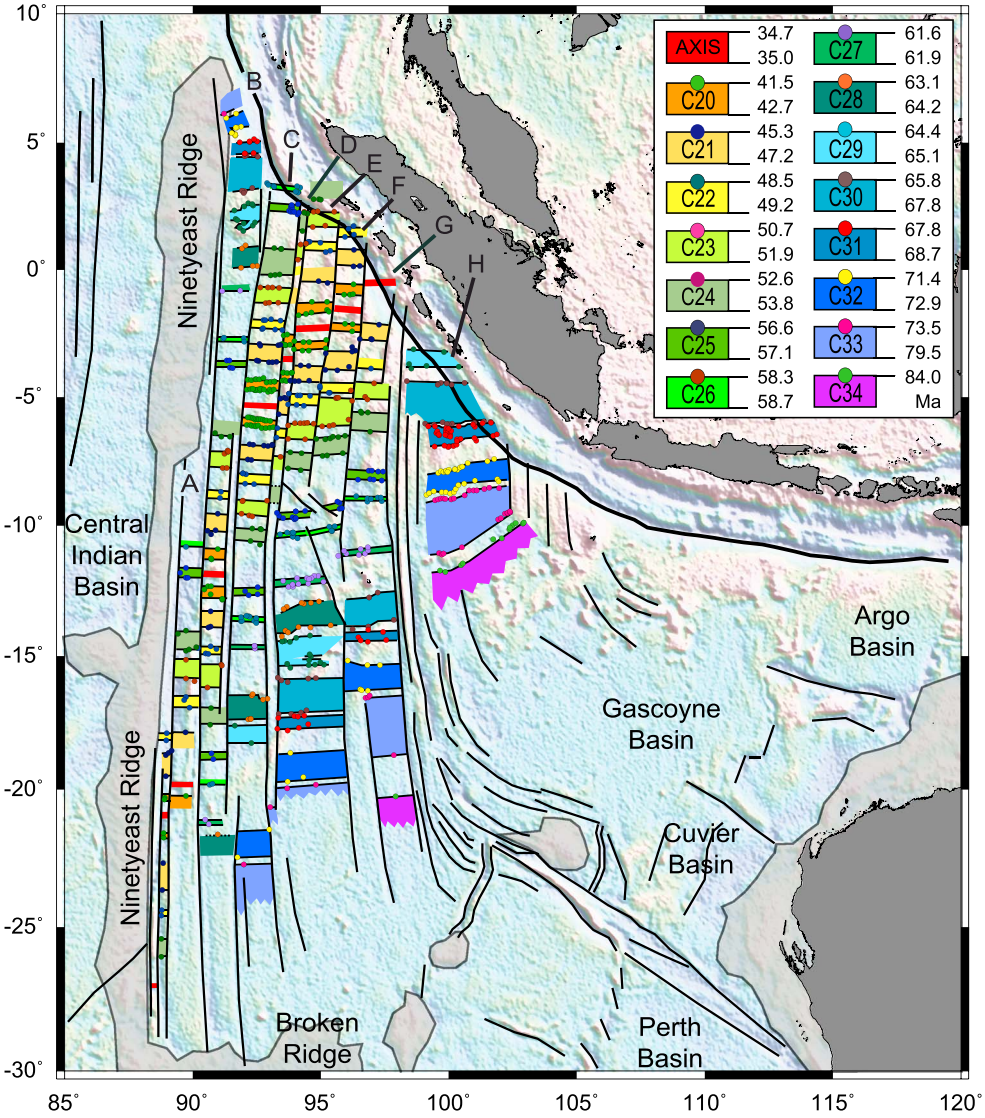

Figure 2. Structure and age of the Wharton Basin deduced from free-air gravity anomaly [*Sandwell and Smith*, 2009; background colors] for the fracture zones (thin black longitudinal lines), and marine magnetic anomaly profiles (not shown) for the isochrons (thin black latitudinal lines). The plain colors represent the oceanic lithosphere created during normal geomagnetic polarity intervals (see legend for the ages of Chrons 20 to 34 according to the time scale of *Gradstein et al*. [2004]). Compartments separated by major fracture zones are labeled A to H. Grey areas: oceanic plateaus, thick black line: Sunda Trench subduction zone.

Wharton Basin. Spreading compartments are narrower toward the Ninetyeast Ridge and wider toward the Investigator Fracture Zone. Some fracture zones were locally reactivated due to active subduction at the Sumatra Trench [*Satriano et al*., 2012; *Meng et al*., 2012; *Yue et al*., 2012; *Delescluse et al*., 2012], or rejuvenated at larger scale due to deformation within the diffuse plate boundary between the Indian, Capricorn, and Somali plates since late Oligocene (20 Ma) [*Deplus et al*., 1998; *DeMets et al*., 2005].

[10] Improving the previous interpretation by *Liu et al*. [1983] and *Royer et al*. [1991], we observe a series of right laterally offset abandoned spreading ridge segments which extend from the Ninetyeast Ridge to the Sunda Trench (Figure 2). East–west trending conjugate anomalies from Chron 20 young (noted 20y; 41.59 Ma) to 26 old (noted 26o; 58.737 Ma) are clearly identified on both flanks of the fossil axis. The trend and shape of the magnetic anomalies observed on the northern flank are similar to those of the magnetic anomalies in the Central Indian Basin [*Sclater and Fisher*, 1974; *Curray et al*., 1982], emphasizing that this northern part belonged to the Indian plate [*Royer et al*., 1991], whereas the southern part was attached to the Australian plate. Due to decreasing spreading rate and increasing tectonic and magmatic complexity, the magnetic anomalies at the fossil spreading center are difficult to decipher. We interpret them as Chron 18y (38 Ma), although it is possible to consider a reduced spreading activity up to Chron 15 (35 Ma) in modeling the observed anomalies. As for the older magnetic anomalies, the sequence continues up to Chron 34y (84 Ma) on the southern flank, although the paucity of data prevents the identification of the oldest anomalies in compartments A to F. On the northern flank, due to its

subduction beneath Sumatra, the basin lacks many isochrons, with lateral variations along the trench.

[11] Compartment H is bounded by the complex Investigator Fracture Zone to the west, and a set of short, poorly defined fracture zones to the east. It is the widest compartment of the basin, with the shortest magnetic anomaly sequence from Chron 29y (64.43 Ma) to Chron 34y (84 Ma). The anomalies within this compartment are progressively realigned from an oblique N60°E trend to an orthogonal east–west trend with respect to the fracture zones. Compartment G displays anomaly sequence from 34y (84 Ma) on the southern flank to the fossil ridge axis, located at the edge of the Sunda Trench. Anomalies 29 and 28 are missing in this compartment, as a result of a southward ridge jump of ~285 km at ~62 Ma; the Cocos Island is located on the scar probably left by this ridge jump. Compartments F and E formed a single wider compartment E-F before Chron 28 (~63 Ma) as seen on the southern flank. During Chron 28, a small segment initiated along the eastern fracture zone and started to grow at the expenses of the main segment. At Chron 26 (~58.5 Ma), these segments display similar lengths. The oblique traces observed in the gravity signal suggest that a faster westward propagation affected the two segments between Chrons 25o and 24o (57–54 Ma), before a stable regime with two segments E and F of similar length established and remained until the spreading ceased in the Wharton Basin. It is worth noting that the ridge jump of compartment G and the subdivision of compartment F and E both happened at about Chron 28 and resulted in replacing a single offset of 325 km between compartments G and E-F by two offsets of, respectively, 96 km between compartments G and F, and 64 km between compartments F and E. Compartments C and B are the longest and most complete ones in the basin. Spreading appears to be continuous and approximately symmetrical from Chron 33y (73.5 Ma) to the spreading cessation. The northernmost part of compartment A is hidden under the Ninetyeast Ridge; nevertheless, Chrons 20y (42.1 Ma) to 26o (58.73 Ma) are observed on the northern flank of the compartment. The southern flank of compartment A and a major part (older than Chron 27) of the southern flank of compartment B remain unconstrained due to the lack of data north of Broken Ridge. The older anomalies identified in compartments C, D, and E-F is Chron 33y (73.5 Ma), although the poorly surveyed southern part of the Wharton Basin located northwest of the Gulden Draak and Batavia knolls probably includes Chrons 33, 33 reversed (33r), and 34 as in the adjacent compartments G and H.

[12] As previous mentioned, single, double, and multiple fracture zones are observed in the Wharton Basin. Magnetic anomaly identification allow us to specify the offset of these fracture zones. The Investigator Fracture Zone is the only multiple one and exhibits a large 900 km offset. The double fracture zones between A-B, B-C, and C–E show 860 km, 710 km, and 310 km offsets, respectively. A few magnetic anomaly identified in the narrow D compartment pinched between the double fracture zone separating C and E suggests that similar offsets exist on each fracture zone of the double fracture zone systems. The single fracture zones between E-F and F-G show a smaller offset of 70 km and 100 km, respectively. The double or multiple fracture zones generally correspond to large offsets (> 300 km), and the single fractures zones to small offsets (< 100 km). The only exception in the Wharton Basin is observed at Chrons 32–30 (73–66 Ma) between compartments E-F and G, when a single fracture zone with a 380 km large offset is observed. This fracture zone, however, proved to be unstable and disappeared when the ridge jump affected compartment G during Chron 28 (~63 Ma). These observations suggest that the double or multiple fracture zones help to sustain large offsets over long period of time, in order to accommodate slight kinematic changes and reduce the friction between large sections of age-deepening lithosphere along the transform fault.

[13] To summarize, the Wharton spreading center has been active between Chrons 34 and 18 (83 to 38 Ma) between the Indian and Australian plates. During this period, its geometry has remained quite stable, with long transform faults offsetting ridge compartments. The ridge segments represent a total length of 1400 km between A and H, whereas the cumulative left-lateral offset reaches a total length of 2300 km. The seafloor spreading in the Wharton Basin ceased at the time of the hard collision of India with Eurasia [e.g., *Patriat and Achache*, 1984], as a consequence of the general reorganization of spreading centers in the whole Indian Ocean. Although India was blocked by Eurasia but subduction continued under Indonesia, the average north–south spreading directions of the Carlsberg, Central Indian, and Southeast Indian ridges rotated eastward. These ridges adjusted to the new spreading direction through rotation or propagation of ridge segments and local ridge jumps. Such an adjustment was impossible, however, in the Wharton Basin, because the long-offset, rigid fracture zones could not accommodate the change. Local ridge jumps to adjust to the new direction were not a solution either, because the Wharton spreading ridge compartments were aligned along the northeast direction, parallel to the new spreading direction. So the spreading ceased in the Wharton Basin, triggering a faster opening between Australia and Antarctica.

4. Plate Reconstructions

[14] A large part of the Wharton Basin is presently missing, subducted under Indonesia. We use the detailed tectonic map described above to reconstruct the past geometry of this missing part. Such a reconstruction can only be done with some accuracy for anomalies conjugate to those which are observed on the southern flank; beyond that, it would be only mere extrapolation. It also requires a proper determination of the finite rotation parameters, pole and angle, describing the relative motion between the Indian and Australian plates for the considered period.

[15] The determination of finite rotation parameters is based on the best fitting of conjugate anomalies and fracture zone segments. The anomalies are real isochrons, whereas the transform faults are not, having been active over a significant period of time depending their offset—a section of a small offset transform fault is active during a short time, a section of a large-offset one during a much longer time. For this reason, constraints from the fracture zones are weighted less than those from the anomalies. In the Wharton Basin, conjugate anomalies are only observed between Chrons 26 and 20. We apply the Hellinger statistical two-plate reconstruction method [*Hellinger*, 1981; *Kirkwood et al.*, 1999]

Table 2. Finite Rotations and Covariance Matrices for the Two Plate Reconstructions of India and Australia (Wharton Basin)

Australia-India	Latitude	Longitude	Angle	$\hat{K}$	a	b	c	d	e	f	g
20y	2.93	9.99	1.15	1.57	0.005	−0.06	0.008	1.12	−0.14	0.03	10^{-5}
20o	2.11	5.84	1.84	0.92	0.008	−0.09	0.01	1.85	−0.24	0.04	10^{-5}
21y	2.42	6.08	3.27	0.81	0.01	−0.10	0.02	1.87	−0.29	0.06	10^{-5}
21o	3.57	−5.48	4.62	0.89	0.02	−0.15	0.03	2.99	−0.56	0.12	10^{-5}
22y	6.18	−9.46	5.88	1.15	0.02	−0.14	0.03	2.91	−0.58	0.13	10^{-5}
22o	5.94	−7.84	6.58	1.21	0.02	−0.23	0.05	3.55	−0.75	0.18	10^{-5}
23y	4.90	−7.88	7.93	1.88	0.01	−0.11	0.02	1.89	−0.32	0.06	10^{-5}
23o	4.57	−7.56	9.09	1.41	0.01	−0.13	0.03	2.34	−0.49	0.12	10^{-5}
24y	7.11	−20.03	11.04	0.55	0.02	−0.05	0.01	0.79	−0.24	0.08	10^{-5}
24o	6.58	−17.77	12.32	2.68	0.02	−0.01	−0.0001	0.98	−0.29	0.11	10^{-5}
25y	6.24	−15.99	15.63	0.91	0.03	−0.22	0.07	6.95	−2.04	0.62	10^{-5}
25o	6.25	−18.37	16.31	1.63	0.07	−0.41	0.13	7.44	−2.19	0.67	10^{-5}
26y	6.36	−17.69	17.91	1.93	0.02	−0.19	0.06	6.8	−2.16	0.706	10^{-5}
26o	6.42	−18.06	18.29	1.34	0.02	−0.24	0.077	6.59	−2.11	0.69	10^{-5}

to reconstruct India and Australia for Chrons 20y (42.1 Ma) to 26o (58.7 Ma).

[16] For older anomalies, however, no direct two-plate reconstruction can be attempted, because we lack conjugate sets of anomalies. To overcome this difficulty, we take advantage of our knowledge of neighboring basins, namely the Central Indian, Crozet, and Australian-Antarctic basins. Conjugate sequences of magnetic anomalies 34 to 26 have been recognized in the Central Indian Basin [*Sclater and Fisher*, 1974] and the Crozet Basin [*Schlich*, 1975, 1982], formed at the fast spreading section of the Southeast Indian Ridge. A reinterpretation based on more complete data sets have been recently achieved [*Yatheesh et al*., 2008, and in preparation, 2014] and reconstructions of the Indian and Antarctic plates have been obtained for this period, both two-plates [*Yatheesh et al*., 2008] and three-plates involving Africa as well [*Cande et al*., 2010]. Conjugate anomalies 34n young (84 Ma), 33n old (79.5 Ma), 32n young (71.5 Ma), 31n old (68.7 Ma), and 27n young (61.6 Ma) have been identified in the Australian-Antarctic Basin on both sides of the slow spreading section of the Southeast Indian Ridge [*Tikku and Cande*, 1999, 2000; *Whittaker et al*., 2007a, J. M. Whittaker et al., Timing of Kerguelen Plateau formation: constraints from plate kinematics and triple junction migration, submitted to *Earth and Planetary Science Letters*, 2011]. Because no clear fracture zone has been identified on this plate boundary, contrasted reconstructions of the Australian and Antarctic plates have been proposed for these periods, with different problems arising aside of the reconstructed area—overlap of Tasmania and Antarctica in *Tikku and Cande* [1999, 2000] model, overlap of the Kerguelen Plateau and Broken Ridge on Whittaker et al. (2007) model.

[17] We use (1) our picks and fracture zone determinations for the Wharton Basin (India-Australia plate boundary); (2) the picks of *Yatheesh et al*. [2008] for the Central Indian and Crozet basins (India-Antarctica plate boundary); and (3) the picks of *Tikku and Cande* [1999] complemented by

Table 3. Finite Rotations and Covariance Matrices for the Three Plate Reconstructions of India, Australia, and Antarctica

Chron	Latitude	Longitude	Angle	$\hat{K}$	a	b	c	d	e	f	g
					Australia-India						
21y	3.32	−1.9	3.21	1.43	0.84	1.51	−0.18	5.53	−0.73	0.13	10^{-5}
24o	6.72	−17.36	11.53	0.11	0.39	1.19	−0.22	4.78	−1.00	0.33	10^{-5}
27y	4.38	−10.79	20.78	0.23	0.06	0.13	−0.04	2.00	−0.83	0.37	10^{-5}
31o	2.92	−5.42	31.15	0.29	0.30	0.06	−0.03	1.2	−0.62	0.37	10^{-5}
32y	3.66	−8.6	33.2	0.03	0.28	0.61	−0.32	2.06	−1.16	0.70	10^{-5}
33o	3.39	−11.22	39.72	0.09	0.20	0.12	−0.06	1.10	−0.66	0.48	10^{-5}
34y	2.30	−5.48	43.48	0.19	0.47	0.46	−0.25	2.43	−1.47	0.94	10^{-5}
					Antartica-India						
21y	13.94	29.24	27.52	0.14	5.18	8.49	−8.37	14.21	−13.72	13.56	10^{-5}
24o	14.75	19.38	33.68	0.08	5.1	8.06	−8.25	12.95	−13.08	13.39	10^{-5}
27y	12.26	15.35	42.45	0.11	4.38	6.78	−7.13	10.67	−11.07	11.66	10^{-5}
31o	9.64	13.79	52.75	0.12	4.36	6.65	−7.10	10.33	−10.85	11.61	10^{-5}
32y	10.37	11.89	54.17	0.04	4.66	7.11	−7.75	11.05	−11.86	13.03	10^{-5}
33o	11.49	8.73	59.80	0.07	4.36	6.64	−7.20	10.33	−10.98	12.02	10^{-5}
34y	8.43	12.73	64.79	0.09	4.75	7.16	−8.01	11.18	−12.17	13.81	10^{-5}
					Antartica-Australia						
21y	14.06	33.37	24.87	0.14	4.20	6.09	−6.37	10.11	−10.47	11.64	10^{-5}
24o	11.92	35.49	25.41	0.08	4.09	6.23	−6.61	9.91	10.15	11.33	10^{-5}
27y	9.01	37.15	25.65	0.11	4.10	6.22	−6.56	9.93	−10.22	10.80	10^{-5}
31o	5.35	38.28	25.72	0.12	4.14	6.15	−6.43	10.06	−10.46	11.23	10^{-5}
32y	4.48	39.11	26.02	0.04	4.07	6.26	−6.55	9.87	−10.25	11.12	10^{-5}
33o	4.84	40.86	26.66	0.07	4.11	6.21	−6.51	9.95	−10.33	11.24	10^{-5}
34y	−0.23	42.59	27.29	0.09	4.11	6.21	−6.46	9.97	−10.43	11.82	10^{-5}

Table 4. Finite Rotation Parameters for the Two Plate Reconstructions of Australia and Antarctica Calculated by the Bullard Contour Fit Method

Chron	Age (Ma)	Latitude (°N)	Longitude (°E)	Angle (Degree)
21y	46.264	13.90	33.3	24.690
24o	53.347	9.6	35.7	25.079
27y	60.920	8.6	37.5	25.482
31o	68.737	7.1	38.1	25.644
32y	71.071	6.6	38.6	25.988
33o	79.075	5.0	39.8	26.471
34y	83.000	5.1	40.9	27.252

Whittaker et al. [2007a, 2007b] for the Australian-Antarctic Basin (Australia-Antarctica plate boundary) to attempt three-plate reconstructions [*Kirkwood et al*., 1999] for Chrons 34y, 33o, 32y, 31o, 27y, 24o, and 21y. The picks located on the Antarctic plate are corrected for the motion having occurred between the Indo-Australian and Antarctic plates since Chron 18o (39.5 Ma) as evaluated by *Royer and Sandwell* [1989], for combination with the Australian and Indian picks in the search for three-plate reconstruction parameters before seafloor spreading ceased in the Wharton Basin. The assumption of spreading cessation at Chron 18o is not accurate, however, as we interpreted it to be at Chron 18y (see above in section 3). The resulting rotations for the India-Antarctica and Australia-Antarctica motions are combined with the finite rotation for the Indo-Australian and Antarctic plates for Chron 18o, in order to obtain finite rotations for the India-Antarctica and Australia-Antarctica motions comparable to those of previous works.

[18] A difficulty in our plate reconstruction exercise is related to the wide deformation zone extending across the Central Indian and northern Wharton Basins as part of the diffuse boundary between the Indian, Capricorn, and Australian plates [e.g., *Royer and Gordon*, 1997; *DeMets et al*., 2005]. Indeed, significant motions have occurred across this diffuse plate boundary, amounting to as much as 125 ± 28 km within the last 11Myr. [*Royer and Gordon*, 1997]. Because the deformation is distributed over a wide area, it is difficult to correct the magnetic anomaly locations for their motion for the last 20 Myr, because such a correction would probably not vary linearly within the deformation zone. For this reason and because the total duration (and therefore the amount) of the deformation is still being debated [*Krishna et al*., 2009], we decided not to make any correction. We anticipate that the effect of the north–south compression in the Central Indian and northern Wharton Basin will have only limited effect on the fracture zone location and will only displace the magnetic anomalies along a submeridian path. All the conjugate magnetic anomalies in the Wharton Basin (i.e., Chrons 26 to 20) are affected by the deformation, and anomalies 34 to 31 in the Central Indian Basin are at least partly located within the deformation zone. The anomalies 21 to 27 in the Central Indian basin lie on the nondeformed lithosphere belonging to the present Capricorn plate. The consequences are the following:

[19] 1. Our three-plate reconstructions will be affected by the deformation of anomalies 34 to 31 in the Central Indian Basin: The India-Antarctica motion will be underestimated, and as a consequence the India-Australia motion will be underestimated as well. No conjugate anomalies exist for these periods in the Wharton Basin, and only fracture zone directions are used to constrain these reconstructions.

[20] 2. Our three-plate reconstructions may be affected by the deformation of anomalies 24 and 21 in the Wharton Basin; for this reason, we decided not to use the magnetic anomalies, and only the fracture zone direction, from the Wharton Basin in these reconstructions. Comparing the predicted location of the anomalies with the real ones will provide an independent mean to estimate the internal deformation between the conjugate anomalies 24 and 21 in this basin.

[21] 3. Our two-plate reconstructions are intrinsically affected by the deformation.

We will discuss the consequence of the deformation zone on the resulting reconstructions in a subsequent subsection.

[22] The statistical two- or three-plate reconstruction method [*Kirkwood et al*., 1999] groups the isochron picks, either magnetic isochrons or fracture zones, by segments locally fitted along great circles: the reconstruction consists in finding the rotation parameters (and uncertainties) that best fit the conjugate great circle segments. This approach has proven ineffective for sets of isochrons lacking a marked fracture zone. Conversely, the Bullard contour fit method, used by *Bullard et al*. [1965] to reconstruct continents [*McKenzie and Sclater*, 1971], proceeds in a different way: each isochron pick of one plate is ascribed a segment of two isochron picks (defining a great circle) on the conjugate plate, and again the reconstruction consists in finding the rotation parameters that best

Table 5. Finite Rotation Parameters of the India-Australia Motion Calculated by the Combination of Motions Between India-Antarctica ("Yatheesh 08" for *Yatheesh et al*. [2008]) and Australia-Antarctica (Various Models: "Tikku 99" for *Tikku and Cande* [1999]; "Whittaker 07" and "Whittaker 11" for *Whittaker et al*. [2007a] and (J. M. Whittaker et al., submitted manuscript, 2011); "Bullard CF" for our Bullard Contour-Fit Reconstruction)

Model Combination		Bullard CF-Yatheesh 08			Tikku 99-Yatheesh 08			Whittaker 07-Yatheesh 08			Whittaker 11-Yatheesh 08		
Chron	Age (Ma)	Latitude (°N)	Longitude (°E)	Angle (Degree)	Latitude (°N)	Longitude (°E)	Angle (Degree)	Latitude (°N)	Longitude (°E)	Angle (Degree)	Latitude (°N)	Longitude (° E)	Angle (Degree)
21y	46.264	15.0	−142.6	35.38	15.2	−142.7	36.27	14.5	−141.3	30.92	14.6	−141.1	30.93
24o	53.347	13.8	−136.6	65.27	14.9	−137.8	71.52	13.1	−135.7	63.69	14.7	−139.0	78.60
27y	60.920	17.0	−137.7	92.83	18.0	−140.1	98.56	13.9	−132.7	77.25	16.8	−139.7	86.73
31y	68.737	19.5	−136.3	100.76	---------	---------	--------	16.7	−131.5	89.82	19.6	−139.3	96.70
32y	71.071	19.7	−138.4	132.17	21.5	−142.8	143.75	15.0	−132.1	121.90	19.3	−138.3	111.07
33o	79.075	18.9	−142.7	168.61	18.7	−143.9	177.41	−12.9	−137.9	179.24	17.9	−141.4	137.46
34y	83.000	−16.3	−151.7	127.01	−15.2	−148.9	138.31	−10.4	−150.6	104.41	14.5	−145.0	177.06

fit the picks and their conjugate great circle segments. Unfortunately, no statistical development based on this approach is available so far, and the resulting rotation parameters lack covariance matrix and confidence ellipsoid. We apply this two-plate method to the Australia-Antarctica magnetic isochron data and obtain an independent set of rotation parameters, computed without any fracture zone constraint.

[23] In a different attempt, we try to constrain the Australia-India motion by using a plate circuit involving Antarctica. To this end, we combine the Australia-Antarctica finite rotation parameters of *Tikku and Cande* [1999]; *Whittaker et al*. [2007a], (J. M. Whittaker et al., submitted manuscript, 2011), or derived from the Bullard contour-fit method, on one hand, and the Antarctica-India parameters from *Yatheesh et al*. [2008], on the other hand.

[24] Table 2 gives the Australia-India finite rotation parameters derived from the two-plate reconstructions, Table 3 the finite rotation parameters derived for all plate boundaries from the three-plate reconstructions, Table 4 the Australia-Antarctica finite rotation parameters derived from the Bullard contour-fit method, and Table 5 the Australia-India finite rotation parameters obtained by various combinations of the Australia-Antarctica and Antarctica-India parameters. Figure 3 displays the resulting three-plate reconstructions. Figures 4 and 5 shows the finite rotation poles for the two- and three-plate reconstructions, with their 95% confidence region (Figure 4) and compared to poles from other studies (Figure 5). Figure 6 presents selected flowlines in the Wharton, Central Indian, Crozet, and Australian-Antarctic basins.

4.1. Finite Rotation Poles

[25] The finite rotation poles of the Australia-India motion obtained by three-plate reconstructions (Figure 4a) are confined within a rather limited area close to 10°W (±8°), 5°N (±3°) for all Chrons between 34y and 21y. These poles are located roughly 90° west of the Wharton Basin: indeed, the long-offset fracture zones of this basin are close to great circles and constrain the poles in a narrow area. The finite rotation poles of the Australia-India motion obtained by two-plate reconstructions (Figure 4b) are generally consistent with the former ones. The better resolution in time, limited to the younger part of the studied period, suggests that the poles cluster in three groups at Chrons 24y–26o (52.6–58.7 Ma), Chrons 21o–23o (47.2–51.9 Ma), and Chrons 20y–21y (41.6–45.3 Ma), with a displacement of 10°, then 15° eastward between the clusters. The finite rotation poles of the Antarctica-India motion obtained by three-plate reconstructions (Figure 4a) present a 20° eastward displacement of the poles from Chron 34 (84 Ma) to 21 (45 Ma). The finite rotation poles of the Australia-Antarctica motion obtained by three-plate reconstructions (Figure 4a) show a regular northwestward migration of the pole over ~15° between Chrons 34 and 21.

[26] Figure 5 is comparing the finite rotation poles deduced from our work with those from other recent works in the same areas. For the Australia-India motion, we limit the comparison to our two- and three-plate reconstructions (Figure 5a): the poles obtained for Chrons 21y (45.3 Ma) and 24o (53.8 Ma) are in good agreement, well inside their 95° confidence ellipses (Figure 4). For the Antarctica-India motion, we compare our poles obtained by three-plate reconstructions of India, Australia, and Antarctica with those of *Cande et al*. [2010] obtained by three-plate reconstructions of India, Antarctica, and Africa on one hand, and with those of *Yatheesh et al*. [2008, and in preparation, 2014] obtained by detailed two-plate reconstructions on the other hand (Figure 5b). Again, the similarity of the pole paths is striking. The three sets of poles are in agreement within less than 300 km, and well inside the 95° confidence ellipses, for Chrons 21y and 24o. The agreement is not so good for Chron 27, although the pole of *Yatheesh et al*. [2008] still lie within the 95° confidence ellipse of ours. Although *Cande et al*. [2010] do not provide rotation parameters for ages older than Chron 29o (65 Ma), the two remaining set of poles are in agreement within less than 300 km, and well inside the 95° confidence ellipses, for Chrons 31o, 32y, 33o and 34y. For the Australia-Antarctica motion, we compare our three-plate reconstruction poles with the two-plate reconstruction poles of *Tikku and Cande* [1999]; *Whittaker et al*. [2007a] and (J. M. Whittaker et al., submitted manuscript, 2011). These three sets of reconstructions differ only by assumptions on the inferred match of poorly defined fracture zones, which remain debated. They result in a poor fit either between Tasmania and Antarctica [*Tikku and Cande*, 1999] or between the Kerguelen Plateau and Broken Ridge [*Whittaker et al*., 2007a]. All four sets of poles (Figure 5c) show a consistent and regular migration of the pole toward the northwest between Chrons 34y and 21y, and a remarkably similar pole for Chron 21y. The pole migration is similar (13 to 14°) for *Tikku and Cande* [1999] and (J. M. Whittaker et al., submitted manuscript, 2011), reaches a much wider amplitude (25°) for Whittaker et al. (2007), with ours in intermediate position (17°). Although *Whittaker et al*. [2007a] and (J. M. Whittaker et al., submitted manuscript, 2011) display rather linear and regular pole paths, *Tikku and Cande* [1999] show a more complex one with a rapid migration, comparable to that of *Whittaker et al*. [2007a], between Chrons 34y and 32y, then a cluster of poles centered on (10°N ±1°, 37°E ±1°) between Chrons 32y and 24o, and finally migration again up to Chron 21y. Our pole path is also sinuous, with inflections at Chrons 33o, 32y, and 27o, as should be expected without fracture zone constraint. The poles derived from the Bullard contour-fit method define a more regular path and compare well with the poles of *Tikku and Cande* [1999] between Chrons 21 and 27 and at Chron 33, and with our three-plate poles at Chrons 21 and between Chrons 27 and 33 (Figure 5).

[27] It should be noted (Tables 2 and 3; Figure 4) that the finite rotation poles for the three pairs of plates, Australia-India, Antarctica-India, and Australia-Antarctica, are all located in a relatively narrow area, between ~20°W and ~45°E and between ~0 and ~15°N. If the poles were coincident, then the angles θ would add such that $\theta_{IND-ANT} = \theta_{IND-AUS} + \theta_{AUS-ANT}$. Indeed the pole paths for Australia-Antarctica and Antarctica-India are progressively converging between Chrons 34 and 21, although their 95% confidence ellipses remain distinct even at Chron 21. This observation is consistent with the evolution of the two distinct plate boundaries to a single boundary between Antarctica and the Indo-Australian plate at about Chron 18. The pole path for Australia-India is also moving toward this location at Chron 20, as shown for the two-plate reconstructions. One may infer that, between Chrons 21 and 18, the three-poles converge, whereas the motion between Australia and India ceases and those between India and Antarctic in one hand, Australia and Antarctic on the other hand, become identical.

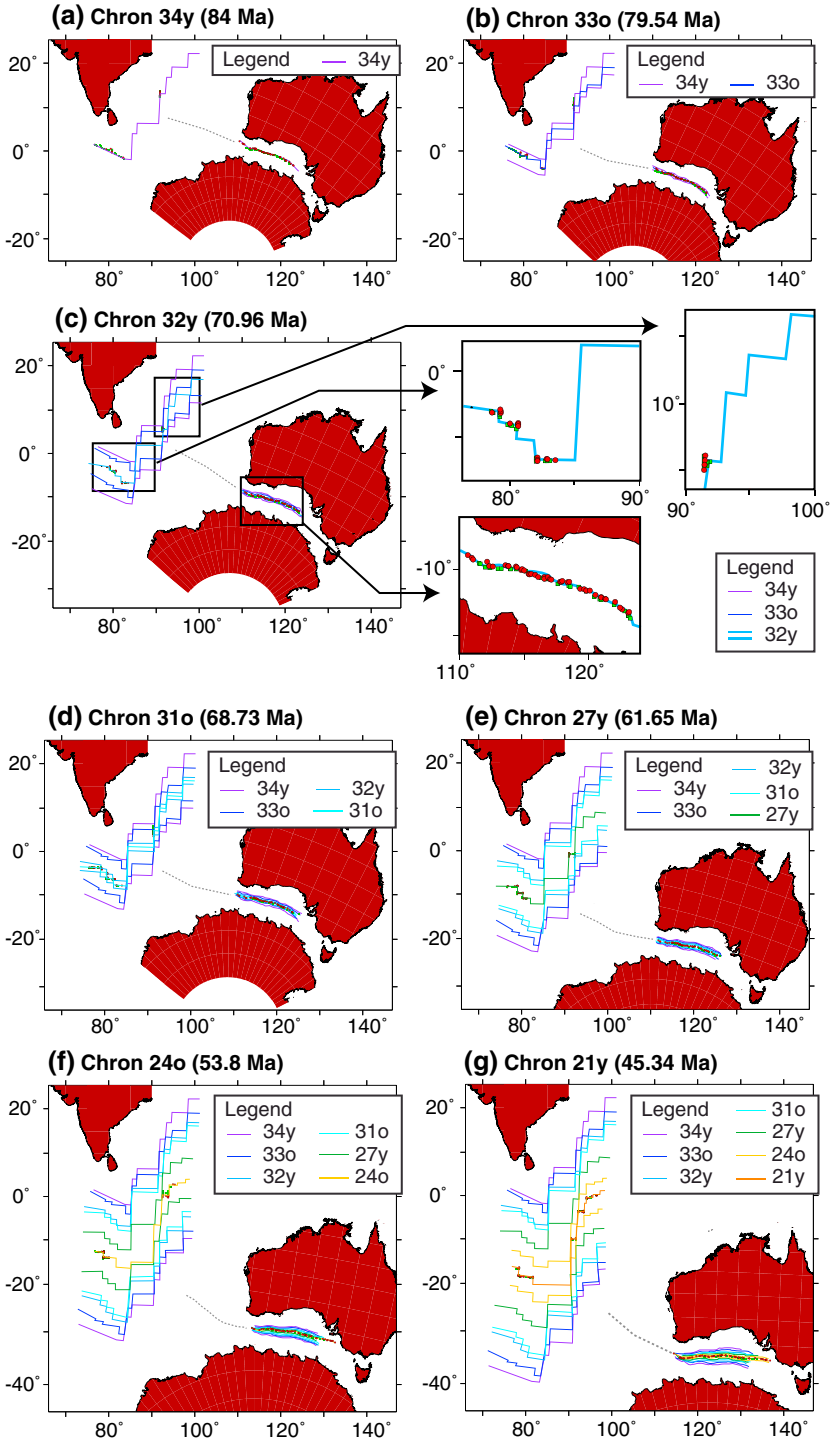

Figure 3. Three-plate reconstructions for (a) Chron 34y (84 Ma), (b) Chron 33o (79.543 Ma), (c) Chron 32y (70.961 Ma), (d) Chron 31o (68.732 Ma), (e) Chron27y (61.650 Ma), (f) Chron 24o (53.808 Ma), and (g) Chron 21y (45.346 Ma). The Indian plate is fixed, the Australian and Antarctic plates are rotated. At each plate boundary, the red circles represent magnetic picks from the northern flank and the green squares magnetic picks from the southern flank. Only picks used in the reconstruction are shown. Isochrons are displayed as thin colored lines (see legend), and active plate boundaries as thick colored lines. Blow-ups of the three plate boundaries and picks are shown for the reconstruction at Chron 32y.

4.2. Reconstructed Flowlines

[28] Flowlines have been derived using these rotation parameters (Figure 6) in order to compare them to the longest fracture zones observed in the basins, when available. In the Wharton Basin (Figure 6a), the flowlines computed from (fossil) ridge location at (11°40′S, 90°27′E) and (5°10′S, 92°4′E) using our detailed two-plate reconstructions of Australia-India motions between Chrons 26o and 18

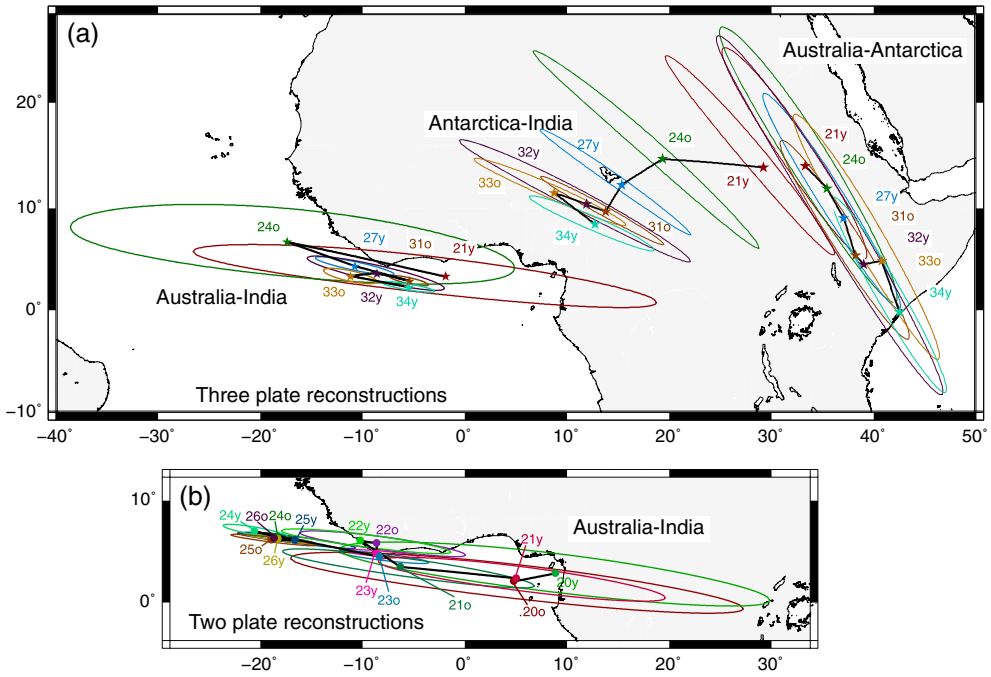

Figure 4. (a) 95% confidence ellipses for the finite rotation poles of the relative motions between Australia and India, Australia and Antarctica, and Antarctica and India, deduced from the three-plate reconstructions for Chrons 21y, 24o, 27y, 31o, 32y, 33o, 34y; (b) 95% confidence ellipses for the finite rotation poles of the relative motions between Australia and India deduced from the two-plate reconstructions for Chrons 20y, 20o, 21y, 21o, 22y, 22o, 23y, 23o, 24y, 24o, 25y, 25o, 26y, and 26o.

consistently fit fracture zones A-B and B-C (named from the nearby compartments) on both the northern and southern flanks of the fossil spreading center. The 95% confidence ellipses are very small, reflecting the good quality of the rotation parameters: they are smaller than the symbol marking the pole for Chrons 18 to 24, and slightly larger for Chrons 25 and 26, with the quality of the rotation parameters decreasing with the available constraints to compute them. The flowlines computed from the same locations using the coarser three-plate reconstructions extending up to Chron 34 also appear to be in reasonable agreement with the fracture zones observed on the gravity data. However, as previously noted, the temporary duplication of the long-offset fracture zones and the creation of intermediate short segments make the comparison quite

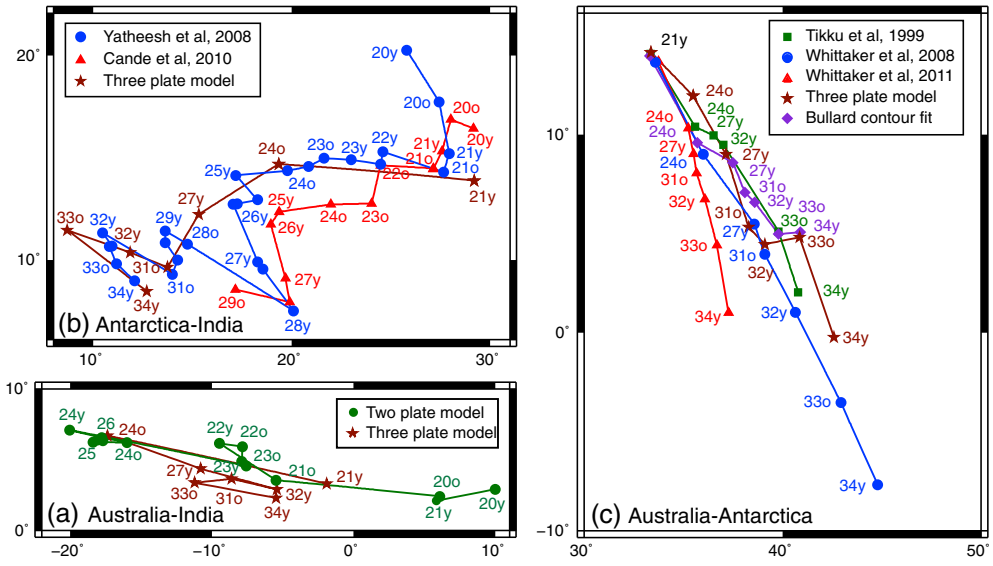

Figure 5. Finite rotation poles of the relative motions between (b) Antarctica and India, (c) Australia and Antarctica , and (a) Australia and India, deduced from our and other two- and three-plate reconstructions (references for the different colors are given in the legend).

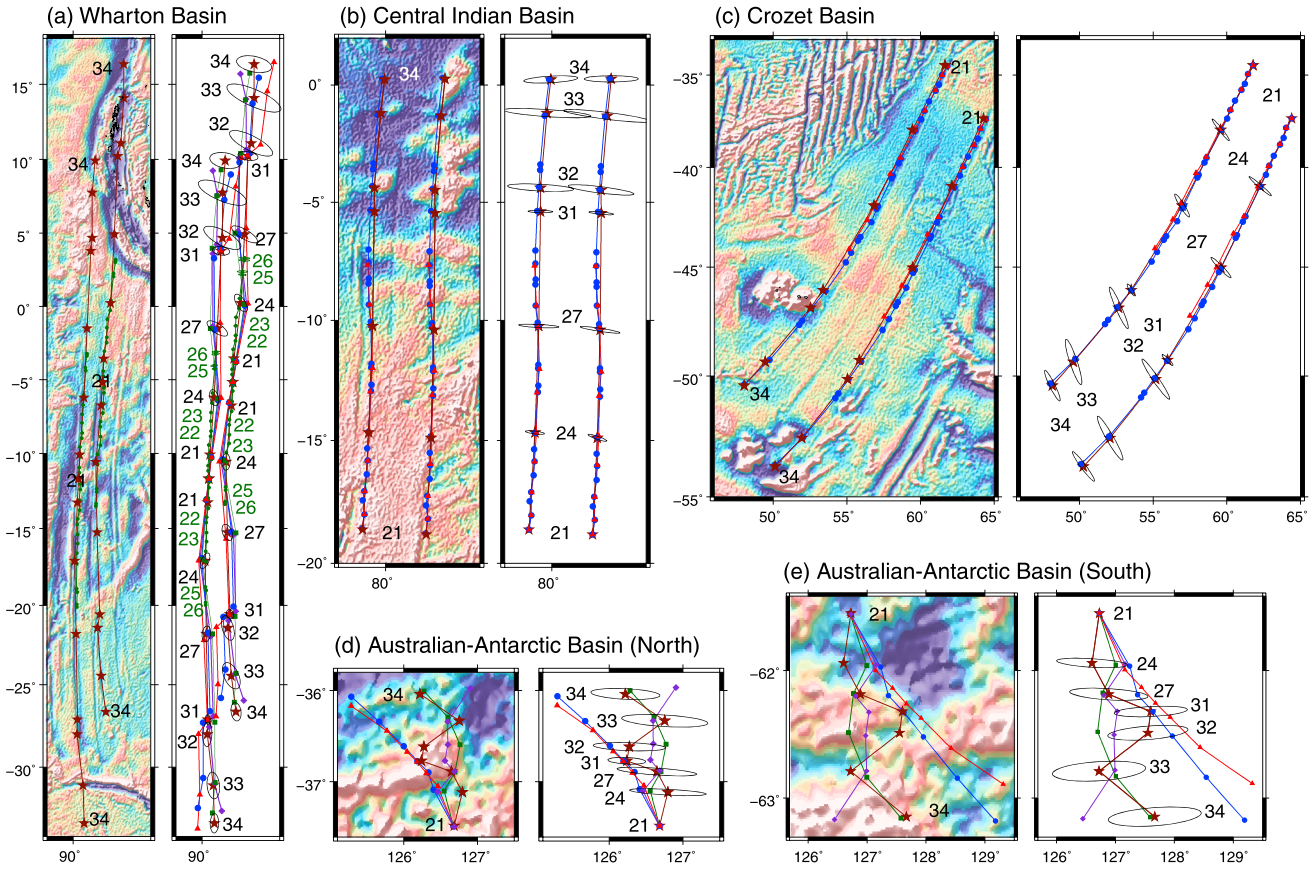

Figure 6. Flow lines computed from the finite rotation parameters deduced from our and other two- and three-plate reconstructions for the relative motions of Australia and India in (a) the Wharton Basin, Antarctica-India in the (b) Central Indian Basin and the (c) Crozet basin, and Australia-Antarctica Basin on (d and e) both flanks of the Australian-Antarctic Basin. The color references of the flow-lines and the age of computed points are both similar to those of the pole paths in Figure 5. Left panels show free air gravity anomaly computed from satellite altimetry [*Sandwell and Smith*, 2009] for comparison of fracture zone traces with the flow lines, right panels show 95% confidence ellipses (in black: three-plate reconstructions, in green: two-plate reconstruction in the Wharton Basin). Additional flowlines in the Wharton Basin results from combined India-Antarctica and Antarctica-Australia motions, the color referencing to those used for the Antarctica-Australia pole paths in Figure 5.

difficult. The 95% confidence ellipse are larger, as expected considering the deformation in the Wharton and Central Indian basins and the poor constraints, limited to the fracture zone data, for the Australia-India motion. The flowlines computed from finite rotation parameters obtained by various combinations of the Australia-Antarctica and Antarctica-India rotations (Table 5) show inacceptable kinks at Chron 24, 31, and 32 (colored lines and symbols on the right panel, Figure 6a). Our three-plate reconstructions provide the most regular flowlines, closely followed by those resulting from the combination of *Yatheesh et al*. [2008] Antarctica-India motions and *Tikku and Cande* [1999] Australia-Antarctica motions. Other combinations, including Australia-Antarctica motions derived from the Bullard contour-fit method and *Whittaker et al*. [2007a], (J. M. Whittaker et al., submitted manuscript, 2011). lead to unacceptable flowlines.

[29] This exercise demonstrates that combining Australia-Antarctica and Antarctica-India motions increases the uncertainties beyond limits on the resulting Australia-India motion, leading us to favor the three-plate approach. Indeed, the fracture zone constraints from the Wharton Basin used in this approach regularizes the solution, unlike the mere combination of rotations along any plate circuit.

[30] For Antarctica-India motion, the flowlines have been computed from two locations of Chron 21, respectively (18°36′S, 79°E) and (18°48′S, 81°42′E) for the Central Indian Basin (Figure 6b) and (34°30′S, 61°49′E) and (37°26′S, 64°26′E) for the Crozet Basin (Figure 6c). The flowlines derived from the detailed two-plate reconstructions of *Yatheesh et al*. [2008], the three-plate reconstructions of *Cande et al*. [2010, involving Africa], and ours (involving Australia) are remarkably similar and fit very well the fracture zones observed on the gravity data. The 95% confidence ellipse are quite large along the trend of the isochrons, reflecting the higher uncertainty assigned to the fracture zone with respect to the magnetic anomalies.

[31] In the Australian-Antarctic Basin, *Tikku and Cande* [1999, 2000] and *Whittaker et al*. [2007a], (J. M. Whittaker et al., submitted manuscript, 2011) applied the two-plate reconstruction method using different fracture zones as a basic

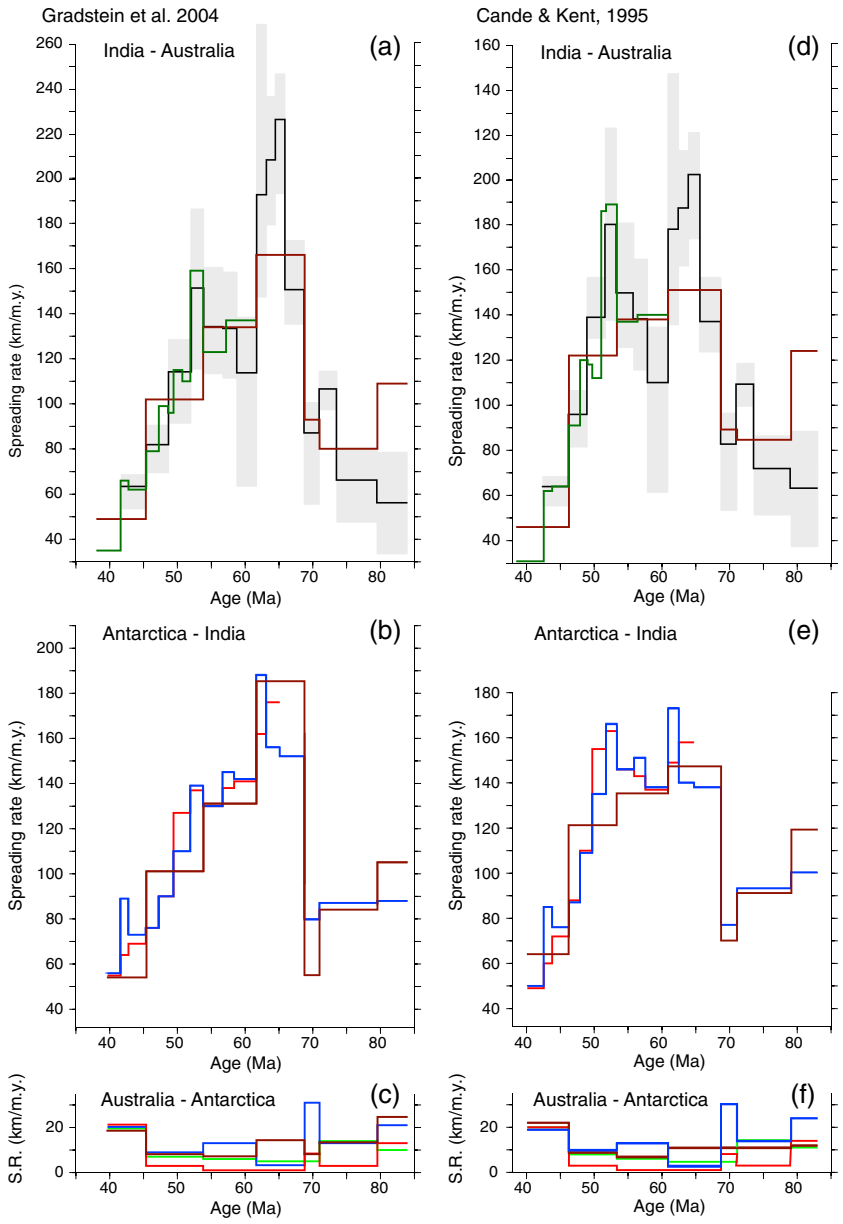

Figure 7. Full spreading rates from the finite rotation parameters deduced from our and other two- and three-plate reconstructions for the relative motion of (a and d) Australia and India, (b and e) Antarctica and India, and (c and f) Australia and Antarctica. The color references of the spreading rate curves are similar to those of the pole paths in Figure 5. The black line represents the spreading rates measured in the Wharton Basin and their uncertainty (standard deviation in grey) To emphasize the dependence of spreading rates to the Geomagnetic Polarity Time Scale (GPTS), the rates are computed for two GPTS.

constraint. We applied the three-plate reconstruction method using the well-defined fracture zones of the Central Indian, Crozet, and Wharton Basins, while excluding the debated fracture zones of the Australian-Antarctic Basin. Our resulting flow lines from Chron 21 at (37°29′S, 126°40′E) on the Australian plate (Figure 6d) and (61°33′S, 126°43′E) on the Antarctic plate (Figure 6e) shows similarities and differences with those derived from the previous works. For instance, our total motion between Chrons 21y and 34y is similar to that of *Tikku and Cande* [1999, 2000] and favors their fracture zone constraint, although our instantaneous motions are only similar to theirs between Chrons 34y and 33o. On the other hand, our total motion between Chrons 21y and 31o is similar to those of *Whittaker et al*. [2007a], (J. M. Whittaker et al., submitted manuscript, 2011), and our instantaneous motions between Chrons 24 and 32 are quite similar in direction and intensity with those of *Whittaker et al*. [2007a], (J. M. Whittaker et al., submitted manuscript, 2011), although they significantly differ between Chrons 21 and 24 on one hand, 32 and 34 on the other one. More generally, our flowlines are more sinuous than those from previous authors, reflecting the lack of fracture zone constraints for the Australia-Antarctica plate

boundary in our three-plate approach. The linearity of this plate boundary, combined with the very slow spreading rate for the period considered, suggests that it may have acted as an accommodation zone for the three-plate system, whereas the India-Antarctica and India-Australia plate boundaries were unable to react to small variations of the forces at the nearby subductions, being somehow "locked" due to their long-offset fracture zones. Indeed, only the major reorganization induced by the "hard collision" of India with Eurasia at ~40 Ma could force the India-Antarctica plate boundary to evolve and reorient by ~50° through local ridge jumps [*Patriat*, 1987], while the India-Australia plate boundary—the Wharton spreading center—became extinct.

[32] The 95% confidence ellipses computed from our three-plate reconstructions are quite large, reflecting the lack of constraints along the isochrons. They demonstrate that the sinuosity of our flowlines for the Australia-Antarctica motion may have little meaning, as a linear trend can be drawn along a N20°W direction cutting across all the ellipses. Moreover, for Chrons 21 to 32 the 95% confidence ellipses barely include corresponding points on all other flowlines. Only for Chrons 33 and 34 are the flowlines from *Whittaker et al*. [2007a], (J. M. Whittaker et al., submitted manuscript, 2011) diverging, and for Chron 34 are those from the Bullard contour-fit method.

4.3. Spreading Rates

[33] Up to this point, our reconstructions only rely on geometrical constraints, i.e., the finite rotation parameters and the derived flowlines remain valid whatever the ages ascribed to the isochrons. However, the spreading rates heavily rely on these ages and therefore on the geomagnetic polarity time scale (GPTS) chosen to date the magnetic anomalies. In order to better appreciate the uncertainties on the spreading rates, We show in Figure 7 the spreading rates computed from the sets of finite rotation parameters presented in Figure 5 using the GPTS of *Cande and Kent* [1995] and *Gradstein et al*. [2004], plotted versus age. The India-Australia and India-Antarctica plate boundaries display a similar evolution, with intermediate spreading rates (around 80 km/my full rate) between ~84–68 Ma followed by very fast rates (120–200 km/m.y.) between ~68–52 Ma and progressively decreasing rates (120 to 40 km/m.y.) between ~52–40 Ma. The Australia-Antarctica plate boundary presents persistently slow spreading rates (lower than 20 km/m.y. full rate) between 84 and 40 Ma. The spreading rates measured from the magnetic anomalies identified in the Wharton Basin and their variations are superimposed on the predicted India-Australia spreading rates (Figure 7, top (black lines and grey areas)). These measured rates agree reasonably well with the predicted ones, except for the period between Chrons 34y and 33y (84–73.5 Ma) for which the predicted rates are systematically higher than the measured ones. We note that the predicted spreading rates for Chrons 34y–33o (84–79.5 Ma) is much higher, about twice the one measured from the observed anomalies. We regard this as a consequence of the poor sampling of isochron 34y in the Crozet Basin, which does not allow us to properly describe the change of spreading direction that happened at that time along the India-Antarctica plate boundary. For this reason, the reconstructions for Chron 34 (and the resulting spreading rates) should be considered with caution.

4.4. Effect of the Diffuse Plate Boundaries Within the Indo-Australian Plate Since 20 Ma

[34] As previously mentioned, our three-plate reconstructions can be separated in two categories with respect to the effects of recent deformation in the Central Indian and Wharton Basins:

[35] 1. For Chrons 34, 33, 32, and 31, the isochrons in the Central Indian Basin are deformed and, because we have no conjugate magnetic anomalies in the Wharton Basin, the only constraint from this basin come from the direction of fracture zone separating compartments A and B. The three-plate reconstructions give good results on the India-Antarctica and Australia-Antarctica plate boundaries (Figures 3a to 3d). The position of the pole describing the Australia-India motion is properly constrained by fracture zone A-B, but the predicted amplitude of the motion is affected by the diffuse plate boundary. Chrons 34 to 31 in the Central Indian Basin are located north of, or within, the deformation zone and lie south of their expected position with respect to Antarctica if the deformation had not happened; therefore, the calculated India-Antarctica motion is underestimated, resulting in a similar underestimation of the Australia-India motion. It should be noted, however, that the Wharton Basin itself has been affected by compression: As a consequence, the Australia-India motion depicted from the distance between observed magnetic anomalies in the Wharton Basin will appear fictitiously slower than the real one. Because the computed poles for the finite and stage rotations of India-Antarctica and Australia-India at anomalies 34 to 31 lie slightly more than 90° to the west of the Wharton Basin, and the finite rotation poles for the India-Capricorn and India-Australia motions across the diffuse plate boundary since 20 Ma lie much closer, about 20° to the west of the Wharton Basin, we expect that the underestimation due to the (smaller) compression in the Central Indian Basin on our three-plate Australia-India motion will be less than the underestimation of Australia-India motion derived from the observed magnetic anomalies affected by the (larger) compression in the Wharton Basin. We can therefore anticipate that the Australia-India motion deduced from the observed magnetic anomalies in the Wharton Basin will be slower than the one computed from our three-plate reconstructions, both of them being slower than the real motion at the time of the formation of the basin.

[36] 2. For Chrons 27, 24, and 21, the isochrons in the Central Indian Basin are not deformed but belong to the Capricorn plate, i.e., the part of the former Indian plate that has not be affected by the recent deformation as long as the India-Antarctica past motions are considered. Anomalies 27 in the Wharton Basin have no conjugate, and the only constraint from this basin at that time come from the direction of fracture zones A-B and B-C. As before, the three-plate reconstruction gives good results on the India-Antarctica and Australia-Antarctica plate boundaries (Figure 3e), and the pole describing the Australia-India motion is properly constrained by the fracture zones. The predicted amplitude of this motion should properly reflect the Australia-India motion at that time. However, because the Wharton Basin has suffered compression during the last 20 Ma, the Australia-India motion deduced from the observed magnetic anomalies in the Wharton Basin will probably appear slower. Conversely, anomalies 24 and 21 have conjugate in the Wharton Basin but lie in the deformed area and were not used in the reconstructions. The misfits between anomalies 24 and 21 reconstructed using the

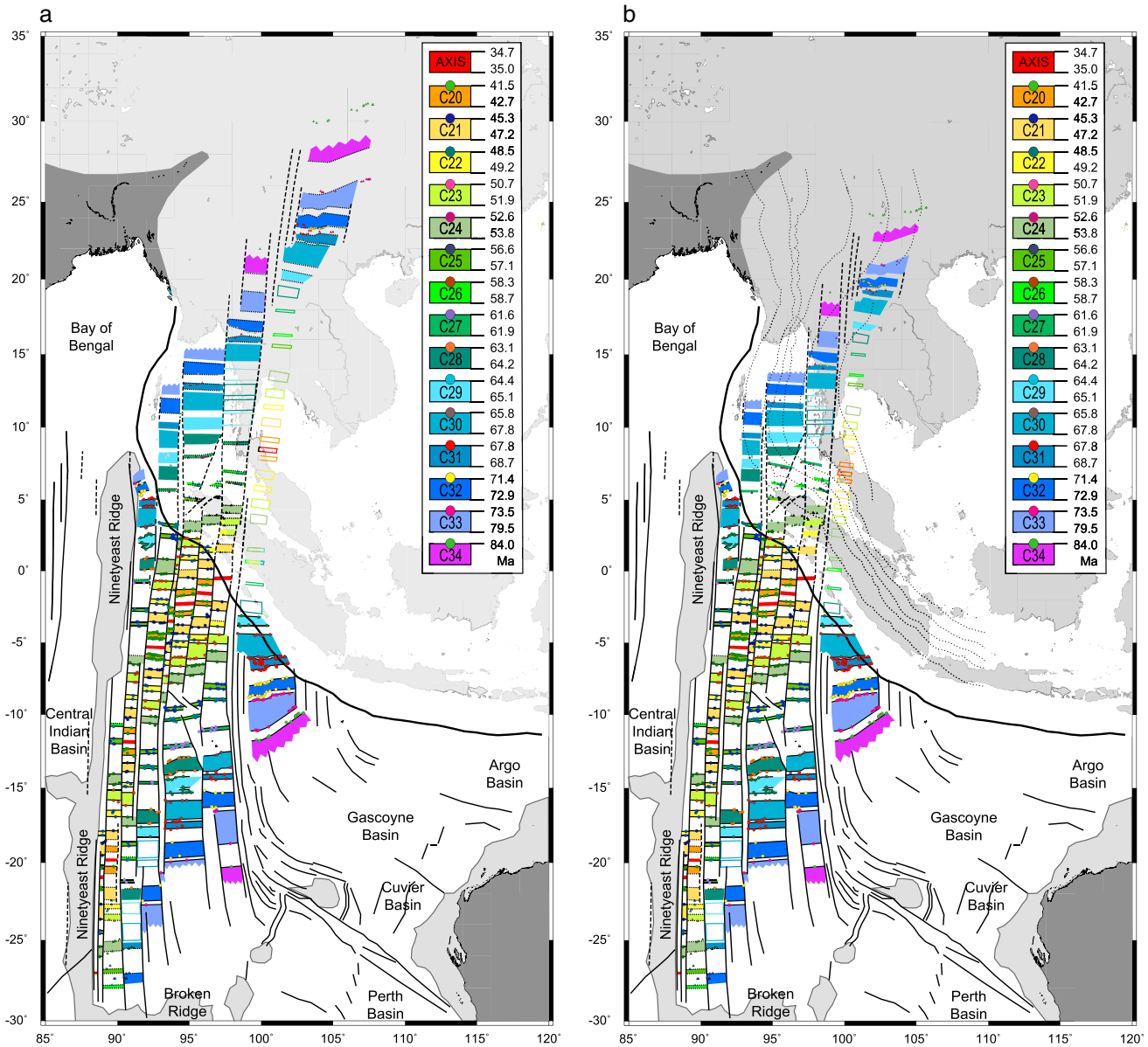

Figure 8. Reconstitution of the subducted magnetic isochrons and fracture zones of the northern Wharton Basin using the finite rotation parameters deduced from our two- and three-plate reconstructions. (a) First the geometry is restored on the Earth surface, then (b) it is draped on the top of the subducting plate as derived from seismic tomography [*Pesicek et al.*, 2010] shown by the thin dotted lines at intervals of 100 km (b). Colored dots: identified magnetic anomalies; colored triangles: rotated magnetic anomalies, solid lines; observed fracture zones and isochrons, dashed lines: uncertain or reconstructed fracture zones, dotted lines: reconstructed isochrons from rotated magnetic anomalies (two-plate and three-plate reconstructions), colored area: oceanic lithosphere created during normal geomagnetic polarity intervals (see legend for the ages; the colored areas without solid or dotted lines have been interpolated), grey areas: oceanic plateaus, thick line: Sunda Trench subduction zone.

best rotation parameters for the India-Australia motion as determined from our three-plate reconstructions are 90 and 7 km, respectively, for a total distance between conjugate anomalies of 1190 and 255 km in compartment C. If the misfit is attributed to the deformation only, this would imply deformation ratios of 7.6 % and 2.7%. These values are very different and would suggest a very heterogeneous deformation. Although it is possible that the area close to the fossil ridge has different rheological properties due to the decreasing spreading rate and ultimately to the spreading cessation (see below in section 5), an alternative explanation exists for such a large difference. As previously mentioned, the exact age of the fossil spreading center remains uncertain and is probably slightly younger than Chron 18o. The small amount of crust

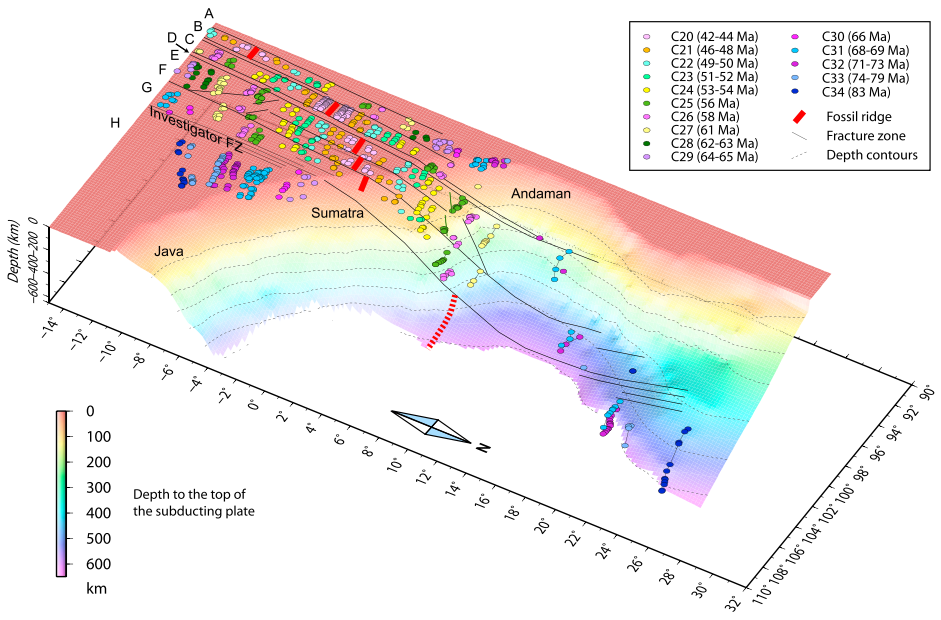

Figure 9. Three-dimensional representation of the subducting northern Wharton Basin, based on our two- and three-plate reconstructions and seismic tomography. Colored circles: identified or reconstructed anomalies, solid lines: observed or reconstructed fracture zones, thick red line: fossil axis (dashed: inferred), background colors and geometry: top of the subducting plate [digitized from *Pesicek et al.*, 2010], thin dotted lines: depth contours of the top of the subducting slab at intervals of 100 km.

formed after Chron 18o at the India-Australia plate boundary is not considered in our three-plate reconstructions, unlike that created after Chron 18o at the India-Antarctica and Australia-Antarctica plate boundaries—we have rotated Antarctic picks to their Chron 18o position with respect to the Indo-Australian plate prior starting the reconstructions. If we assume a constant deformation rate α in the central part of the diffuse plate boundary, where both anomalies 24 and 21 lie, the observed misfit for each chron, δ_x ($x = \{24,21\}$) is the sum of the errors caused by the deformation and by the poor evaluation of the spreading cessation age, i.e.,

$$\delta_{24} = \alpha\, d_{24-24} + d_{18-18}$$

$$\delta_{21} = \alpha\, d_{21-21} + d_{18-18}$$

where d_{18-18} is the distance between conjugate anomalies 18o (i.e., the amount of crust younger than Chron 18o). Solving the above relationships results in α = 9% and d_{18-18} = 15 km. Applying this deformation ratio to the whole deformation zone, about 2000 km wide, would result in a relative motion of 180 km across the diffuse plate boundary. This value is higher than the one obtained by *Royer and Gordon* [1997], 125 ± 28 km, but they do not take possible deformation prior 11 Ma [*Krishna et al.*, 2009]. Also. the deformation ratio is probably not constant all across the diffuse plate boundary but decreases toward its edges, which would make both results compatible. The amount of crust created after Chron 18o at the India-Australia plate boundary is minor: Assuming an ultraslow spreading rate of 5 km/Myr would then make the Wharton Basin fossil ridge 3 m.y. younger, i.e., 36.5 Ma (about Chron 17y); assuming a rate of 10 km/Myr would make the spreading to cease at Chron 18y, as suggested in section 3.

4.5. Reconstructed Geometry of the Subducted Wharton Basin

[37] Figure 8a presents the reconstructed Wharton Basin based on the three-plate reconstructions discussed above. On this figure, the reconstructed northern flank is shown in its original configuration, prior subduction. Compartments A to G (i.e., west of the Investigator Fracture Zone) display continuous sequences of Chrons 34 to 18. Compartment H, east of the Investigator Fracture Zone, only shows conjugate Chrons 34 to 29, due to the lack of observed younger anomalies in the Wharton Basin. We do not know if the subduction of the spreading axis in this compartment predated or postdated the cessation of spreading slightly after 39.5 Ma. Assuming that seafloor spreading was symmetrical in this compartment since Chron 31o, the spreading axis would be located about 1300 km away from the subduction zone. Assuming that the current subduction rate under southern Sumatra has been constant at about 45 km/Myr, it would have taken approximately 30 Myr to consume the oceanic lithosphere separating the spreading axis to the present trench. So it is most likely that spreading cessation predated subduction of the fossil spreading axis by about 10 Myr in compartment H. The inferred location of the fossil axis is shown by a dashed line on Figure 8a. We do not present interpolated chrons in compartment H, since, unlike the other compartments, we do not know the details of any spreading complexity in this compartment.

[38] Despite our efforts, the reconstructed Wharton Basin presented in Figure 8a should only be regarded as an approximation. Indeed, the uncertainties imposed by the presence of the diffuse plate boundary extending across the Central Indian and Wharton Basins generate errors in the rotation parameters and therefore in the rotated picks. These errors vary

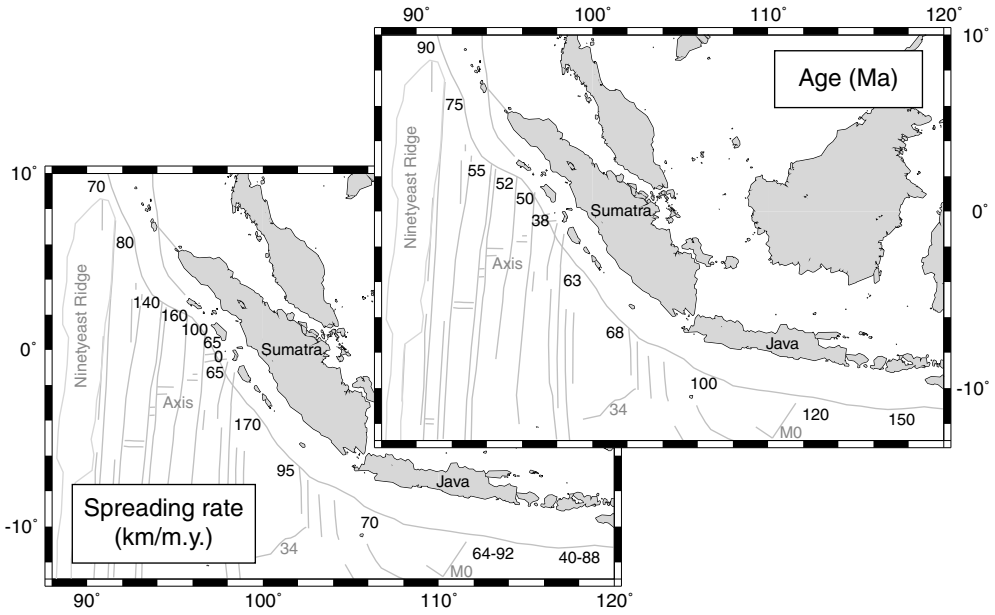

Figure 10. (bottom left) Varying age and (top right) spreading rate of the Wharton Basin lithosphere along the Sunda Trench.

among the different chrons and result, once the rotated picks are combined, in apparent spreading asymmetries that are likely to be fictitious. Such may be the case of the reconstructed Chrons 33o and 34y of the northern Wharton Basin, which are separated by a distance much wider than that observed on the real anomalies of the southern flank—although some asymmetry has likely existed to explain the unusually close observed anomalies 33o and 34y in compartment H. We regard these problems as inherent to the lack of constraints and complexity of the problem.

[39] Figure 9 is showing a perspective view, looking south, of the northern part of the reconstructed Wharton Basin superimposed on the geometry of the subducting plate as imaged by seismic tomography. The tomographic model of *Pesicek et al*. [2010] was digitized slice by slice and smoothed in order to get a realistic topography of the subducting plate. The fracture zone geometry and the magnetic picks were draped on this topography assuming that the direction of subduction, about N18°E, did not deviate from the present one. This image suggests that the fossil ridge in compartment H has reached the depth of 500–600 km. The direction of subduction is oblique with respect to the fracture zones. Although the NS subducting fracture zones seem to deepen up to ~14°N and then get shallower northward, the subducting lithosphere is progressively deepening along N18°E, the direction of subduction. The peculiar geometry of these subducted fracture zones beneath the Andaman Sea may create zones of weakness, favoring the subducted lithosphere to fold and/or break at large scale, as suggested by *Pesicek et al*. [2010].

[40] Figure 8b is showing a map view of the reconstructed Wharton Basin once the geometry of fracture zones and magnetic picks are projected onto the subducting plate deduced from the seismic tomography. It can be seen as a combination of Figures 8 and 9. Although subduction of the spreading axis is most likely to postdate spreading cessation in compartment H, this is probably not the case of past compartments of the Wharton Basins located further east. These compartments were probably offset from compartment H by a major fracture zone, as suggested by the gravity signature deciphered off the Sunda Strait. Therefore, it is likely that in these compartments the Wharton spreading center subducted beneath Eurasia prior to the spreading cessation at ~39.5 Ma. The subduction of an active spreading center is known to create slab windows (e.g., Chili Ridge south of the Chili Triple Junction) and may even lead to the creation of new plate boundaries (see *Bourgois and Michaud* [2002], for a review of such processes off Chili and Mexico). The slab window opened by segments of the Wharton spreading center subducted prior to 39.5 Ma, inferred to be as large as 1500 km [*Whittaker et al*., 2007a], likely affected the convective circulation in the asthenosphere and may have played a role in the early Cenozoic magmatism of South China and Indochina, which exhibits Indian-type isotopic signature [*Fedorov and Koloskov*, 2005], and in the initial opening of the South China Sea before Chron 11 at ~32 Ma [*Briais et al*., 1993; *Barckhausen and Roeser*, 2004].

5. Variations of the Subducting Plate, Consequences on the Subduction Processes

[41] The physical properties, structure and composition of the subducting oceanic lithosphere have important consequences on the subduction processes and their variation along the trench may induce lateral variation in the subduction patterns. The age of the oceanic lithosphere is an important parameter [e.g., *Ruff and Kanamori*, 1980] as it determines the thickness and buoyancy of the subducting lithosphere, hence its ability to comply with or resist subduction. The spreading rate at which the oceanic lithosphere was formed has implications on the structure and composition of the oceanic crust, and therefore on its rheology. Other peculiarities such has the presence of fracture zones or seamounts may also affect the subduction.

5.1. Age of the Subducting Lithosphere

[42] The age of the oceanic lithosphere subducting in the Sunda Trench displays important variations along the subduction zone (Figure 10). This parameter varies progressively within each spreading compartment, with jumps at each fracture zone. On the northern flank of the fossil axis, north of the equator, the age of the subducting crust decreases southeastward from 75 Ma in compartment B to 55 Ma in compartment C and 38 Ma in compartment G, the youngest age being reached where the fossil spreading axis enters the subduction zone. On the southern flank of the fossil axis, south of the equator, this age increases southeastward to 63 Ma immediately east of the Investigator Fracture Zone to 68 Ma east of compartment H. Older ages are observed further east, with ~120 Ma off eastern Java, where anomaly M0 has been recognized in the Gascoyne Basin, and ~150 Ma off Sumba Island, where anomalies M22 have been identified in the Argo basin [*Sager et al*., 1992].

[43] It has long been observed that the bathymetry of normal oceanic lithosphere deepens with age, and its heat flow decreases. Two classes of thermal evolution models have been proposed to explain these observations: the half-space cooling models, which consider a succession of hot intrusions at ridge axis progressively cooling as they move away from the axis, and the plate cooling models, which additionally impose a constant temperature at the base of the plate to reflect asthenospheric convection [e.g., *Parsons and Sclater*, 1977; *Stein and Stein*, 1992]. In the plate model, the additional heat transfer is only effective at old ages, and therefore a third class of models, the CHABLIS models (for "Constant Heat-flow Assigned on the Bottom Lithospheric Isotherm") considers additional heat transfer for all ages [*Doin and Fleitout*, 1996]. Although the plate cooling had once been favored on their better fit to the bathymetric and heat flow data [*Parsons and Sclater*, 1977; *Stein and Stein*, 1992], recent works support either a half space model assuming temperature-dependent mantle properties [*Korenaga and Korenaga*, 2008], a CHABLIS model [*Goutorbe*, 2010] or a plate model [*Hasterok*, 2013] on different considerations. Whatever the correct model, the bathymetry can be approximated by a law in $\sqrt{t}$ for ages t younger than 70 Ma, as expected for the half-space cooling models, and flattens toward an asymptotic for older ages [*Parsons and Sclater*, 1977; *Stein and Stein*, 1992].

[44] Within the assumptions of the half-space cooling models, the thickness of the oceanic lithosphere is linearly related to the square root of its age. For instance, *Turcotte and Schubert* [1982] propose the relation $z_l = 2.32\sqrt{\kappa\, t}$ where κ is the thermal diffusivity (about 10^{-6} $m^2 s^{-1}$), t is the age (in s), and z_l is the thickness of the lithosphere (in m). We apply this relationship to the lithosphere subducting under Indonesia, weighted by the ratio $\frac{d_p(t)-d_0}{d_{h(t)}-d_0}$, where $d_p(t)$ and d_0 are the depths at ages t and zero in the plate model GDH1 of *Stein and Stein* [1992] and $d_h(t)$ the depth at age t in the half-space model approximation of *Parsons and Sclater* [1977, equation (21)] for ages younger than 70 Ma. As expected, this ratio is close to 0.95 at 70 Ma and decreases to 0.7 at 160 Ma. The oceanic lithosphere thickness varies from 105 km in compartment B to 97 km in compartment C and 85 km in compartment G, the thinnest lithosphere being predicted where the fossil spreading axis enters the subduction zone. The lithospheric thickness increases southeastward to 101 km immediately east of the Investigator Fracture Zone to 103 km east of compartment H. Further east, it may reach 113 km off eastern Java and 115 km off Sumba Island. So in first approximation the lithospheric thickness increases by ~25% on the northern flank of the fossil ridge, and by ~35% on its southern flank.

[45] The bulk density of the lithosphere varies with its thickness. The lithosphere is made of (1) the crust, formed at the ridge axis, in average ~7 km thick for all ages [e.g., *White et al*., 1992] and with a mean density of 2860 $kg\,m^{-3}$ [e.g., *Carlson and Herrick*, 1990], and (2) the lithospheric mantle, which amount for the remaining part of the lithosphere, has a varying thickness and a mean density of 3300 $kg\,m^{-3}$. Subduction is happening because the cooler lithospheric mantle is denser than the warmer asthenospheric mantle (density ρ_a of ~3250 $kg\,m^{-3}$). The bulk density of the lithosphere ρ_l varies with the proportion of lithospheric mantle, and therefore with the age [*Stern*, 2002]. In the Sunda Trench area, under the above assumptions, the bulk density of the lithosphere varies from 3264 $kg\,m^{-3}$ at the fossil spreading center (38 Ma) to 3268 $kg\,m^{-3}$ in compartment C and 3271 $kg\,m^{-3}$ in compartment B northwestward, and to 3270 $kg\,m^{-3}$ in compartment H, and 3273 $kg\,m^{-3}$ off Eastern Java and further east.

[46] We define the "subductability" of the lithosphere as $S = g\,(\rho_l - \rho_a)\,z_l$, where g is the acceleration of the gravity (~9.81 $m\,s^{-2}$). This parameter represents the extra weight applied on the asthenosphere by the part of the bulk lithospheric density exceeding the asthenospheric density. A negative subductability means that the bulk lithospheric density is lower than the asthenospheric density, i.e., the plate will resist subduction, which is the case for lithosphere less than ~23 Ma. Along the Sunda Trench, the subductability varies from 1.2 10^9 $N\,m^{-2}$ on the fossil ridge to 1.7 10^9 $N\,m^{-2}$ on compartment C and 2.1 10^9 $N\,m^{-2}$ on compartment B northwestward, and to 2.0 10^9 $N\,m^{-2}$ on compartment H, 2.5 10^9 $N\,m^{-2}$ off Eastern Java, and 2.6 10^9 $N\,m^{-2}$ off Sumba southeastward.

[47] The general morphology of the Sunda Trench and fore-arc is in good agreement with our subductability. The eastern part, off the southernmost Sumatra, Java and eastward, corresponds to oceanic lithosphere older than 100 Ma which presents a higher subductability; this area exhibits a deep trench (deeper than 6000 m) and no fore-arc islands. The northwestern part, off Sumatra and Nicobar Islands, corresponds to oceanic lithosphere formed between 80 and 38 Ma and has a lower subductability; this area exhibits a shallower trench (although the sedimentary influx, decreasing along the trench from north to south, should also be considered) and a set of fore-arc islands. The presence of these islands and their elevation may directly reflect the age (and therefore the subductability) of the subducting lithosphere (P. Tapponnier, personal communication, 2012), although their geology appears to be complex [e.g., *Samuel et al*., 1997].

[48] Neither variations in the crustal thickness nor variations in sediment thickness have been considered in estimating the subductability. Local variations of the crustal thickness have been depicted from seismic data in compartments C–E. The crust formed there between 55 and 58 Ma appears to be extremely thin, less than 4.5 km thick, possibly as an effect of the Kerguelen hotspot [*Singh et al*., 2010], but this thin crust

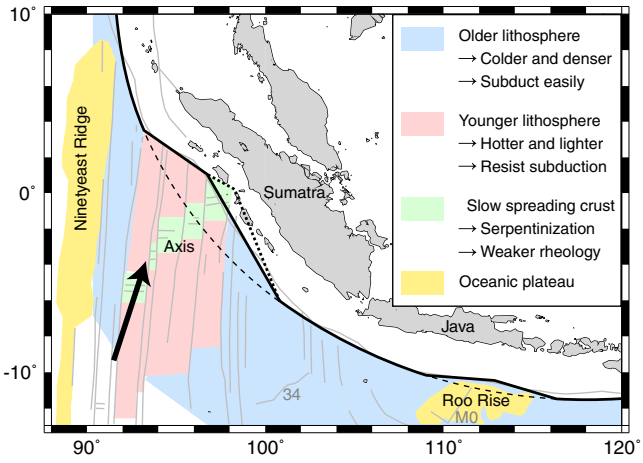

Figure 11. The deviation of the Sunda Trench from a regular arc shape (dotted lines) off Sumatra is explained by the presence of the younger, hotter and therefore lighter lithosphere in compartments C–F, which resists subduction and form an indentor (solid line). The very young compartment G was probably part of this indentor before oceanic crust formed at slow spreading rate near the Wharton fossil spreading center approached subduction: The weaker rheology of outcropping or shallow serpentinite may have favored the restoration of the accretionary prism in this area. Further south, the deviation off Java is explained by the resistance of the thicker Roo Rise, an oceanic plateau entering the subduction.

does not significantly change the bulk buoyancy of the oceanic lithosphere. Similarly, the sediment thickness in the Wharton Basin decreases from 3 km off Northern Sumatra to ~1 km off Central Sumatra, remains less than 1 km off Southern Sumatra and Java, and increases to ~1 km off Sumba [*Laske and Masters*, 1997]. These variations do not significantly alter the bulk buoyancy of the oceanic lithosphere but likely have an effect on the amount of sediments driven to subduction and the size of the accretionary prism.

5.2. Structure and Composition of the Subducting Lithosphere: Effect of the Spreading Rate

[49] The spreading rate and the temperature of the asthenosphere play a major role in the style of crustal accretion at midocean ridges [e.g., *Chen and Morgan*, 1990]. Fast/hot spreading centers, presently observed along the East Pacific Rise, are characterized by axial domes and a smooth bathymetry; they generate a layered magmatic crust including a thick and continuous basaltic layer. Slow/cold spreading centers, presently observed along the Mid-Atlantic Ridge, display an axial valley and a rough bathymetry; they generate a complex crust including discontinuous basaltic and gabbroic patches as well as serpentinized peridotites [e.g., *Macdonald*, 1982; *Gente et al*., 1995; *Cannat*, 1993; *Cannat et al*., 2006]. On the present ridges, the threshold between axial domes and valleys is generally observed for a full spreading rate of 70 km/Myr. Only a few areas of anomalously hot mantle (e.g., Reykjanes Ridge near Iceland) exhibit an axial dome and a smooth topography at a slow spreading rate, and only one area of anomalously cold mantle (Australian-Antarctic Discordance) exhibits a marked axial valley and a rough topography at an intermediate to fast spreading rate. In the following parts, we assume for simplicity that the type of oceanic crust depends on the spreading rate and refer to crust formed at slow (fast) spreading rate as "slow crust" ("fast crust").

[50] In a subduction zone, the contact between the subducting and overriding plates is often considered to be the top of the oceanic crust and the overlying sediments. The roughness of this interface and the rheology of its constitutive material are essential parameters constraining the slip of the downgoing plate in the seismogenic zone, and therefore the characteristics of the resulting earthquakes. It is unfortunately difficult to predict whether the presence of slow or fast crust will ease or resist the motion. Indeed the rough topography of a slow crust may offer more asperities, and therefore a more irregular slip, than the smooth topography of a fast crust. Conversely, the weak rheology of serpentines present in a slow crust would favor a regular slip, unlike the brittle magmatic rocks of the fast crust and the underlying dry olivine mantle.

[51] The lithosphere subducting in the Sunda Trench was formed at different spreading rates, as shown by Figure 7 (top). An intermediate spreading rate (between 60 and 90 km/Myr full rate—a typical intermediate rate is 70 km/My) has prevailed between Chrons 34y and 31o (84–69 Ma), despite the uncertainties on Chron 34y (see previous section). A fast spreading rate (above 90 km/My) is observed between Chrons 31o and 22y (69–48.5 Ma)—the later age being given by the two-plate reconstructions. The spreading rate decreased rapidly from 80 (or 90 km/My depending on the GPTS) between Chrons 22y to 21y (48.5–45.3 Ma) to 35 (or 30 km/My depending on the GPTS) between Chrons 20y and 18y (41.6–38 Ma), then to zero at Chron 18y or slightly after. For times older than Chron 34, a spreading rate of 70 km/My can be inferred from the identifications of anomalies 34 (84 Ma) and M0 (~120 Ma) in compartment H and southeastward, despite the change of spreading direction at ~100 Ma. Full spreading rates of 64–92 km/My have been reported in the [*Mihut and Müller*, 1998] and of 40–88 km/My in the Argo Basin [*Sager et al*., 1992].

[52] The oceanic lithosphere subducting along the Sunda Trench was formed at various spreading rates, ranging from slow (0–60 km/Myr) around the Wharton fossil spreading center in compartment G off Nias, to intermediate (60–90 km/Myr) at some distance of the Wharton fossil spreading center in compartments G, in compartment B off Nicobar and further north, and east of compartment H off the Southernmost Sumatra, Java, up to Sumba islands, to fast (90–170 km/Myr) in compartments C–F and in compartment H. The repartition of spreading rates is therefore quite symmetrical with respect to the fossil ridge, evolving from intermediate in the oldest lithosphere far from the fossil ridge to fast at about 500 km from the fossil ridge to intermediate near, and slow at, the fossil ridge.

[53] The subducting lithosphere was mostly formed at intermediate to fast spreading rates, with the notable exception of compartment G which displays lithosphere created at slow rates. The gravity anomaly derived from satellite altimetry [*Sandwell and Smith*, 2009] exhibits a smooth signature within most of the Wharton Basin, suggesting that the basin was formed at an axial dome similar to that of the present fast East Pacific Rise or intermediate Pacific-Antarctic Ridge. We may therefore expect a smooth topography and a magmatic oceanic crust made of continuous basaltic and gabbroic layers. Conversely, a band 200 km wide centered on the

fossil spreading center was probably formed at an axial valley similar to the present slow Mid-Atlantic Ridge. There we do anticipate a rougher topography and a discontinuous magmatic crust, with possible outcrops of deep crustal and mantle rocks. Indeed, a bathymetric survey of the Wharton fossil ridge in compartment C shows that, despite the abundant sedimentary infill, the axial topography emerging from the sediments is irregular and segmented [*Hebert*, 1998; *Hebert et al*., 1999], an observation confirmed by the gravity anomaly in other compartments.

[54] These observations suggest that the only place where slow spreading rates may significantly change the properties of the subducting lithosphere is within 200 km of the fossil spreading center, i.e., in compartment G. Adding this effect to the effect of lithospheric age allows us to build a conceptual model to explain the geometry of the subduction zone off Sumatra. The general shape of the Sunda Trench is a regular arc, the center of which would be located north of Borneo. However, the trench displays an additional regional sinuosity near Sumatra. Figure 11 clearly shows that, by comparison to the regular arc, the trench is progressively displacing inward between the fracture zone separating compartments B and C and the fracture zone separating compartments F and G, where it reaches 250 to 300 km, before returning to the regular arc in the middle of compartment H. We explain this displacement by the resistance of the younger, warmer, and therefore more buoyant oceanic lithosphere of compartments C to F against the subduction. As a result, this section of subducting lithosphere behaves as an indenter and pushes the accretionary prism forth and up, creating the Sumatran fore-arc islands. The case of compartment G is slightly different: A few million years ago, when intermediate to fast young lithosphere was involved in the subduction, it was probably similar to compartments C to F and therefore the indentation may have extended further east. However, the presence of slow lithosphere—involving a discontinuous magmatic crust and serpentinized upper mantle rocks—in the subduction probably weakens the friction on the subduction plane and facilitate the restoration of the accretionary prism above compartment G, resulting in the present geometry.

[55] We therefore consider that three parameters, (1) the variation in buoyancy related to the age of the lithosphere, (2) the variation in rheology related to the spreading rate at which it was formed, and of course (3) the variation of the sediment cover thickness, play a major role in shaping the accretionary prism off Sumatra. Indeed the width of the accretionary prism, either defined as the distance from the frontal thrust to the back thrust next to the fore-arc basin (W_1) or as the distance from the frontal thrust to the continental mantle wedge (W_2), decreases from compartment B (seismic section WG2) [*Singh et al*., 2012, $W_1 \sim 182$ km and $W_2 \sim 148$ km] to compartment E (seismic section WG1) [*Singh et al*., 2008; *Klingelhoefer et al*., 2010, $W_1 \sim 176$ km and $W_2 \sim 138$ km], and further to compartment F (seismic section BGR06-135) [*Shulgin et al*., 2013, $W_1 \sim 142$ km and $W_2 \sim 126$ km], before increasing in compartment H (seismic section CGGV 940) [*Singh et al*., 2011, $W_1 \sim 160$ km and $W_2 \sim 142$ km]. The seismic sections do not show evidence of a more active, widespread subduction erosion in the narrower part of the prism, and most of the reduction in width may have been compensated in height, resulting to the emergence of the fore-arc islands and the shallow bathymetry of the area [e.g., *Franke et al*., 2008].

5.3. Structure and Composition of the Subducting Lithosphere: Other Effects

[56] In the previous sections we described the effects of age and spreading rate that affect large areas of oceanic lithosphere. Specific features may also have a local effect on the subduction. Fracture zones are preferential areas for outcropping (or shallow) mantle rocks. Such rocks alter to serpentinite and acquire a weaker rheology which would favor aseismic slip on the subduction plane. The multiple Investigator Fracture Zone, which lies just east of compartment G, may superimpose such an effect to that of the slow spreading lithosphere described in the previous section.

[57] A subducted seamount has been identified in the Sumatra area between Enggano Island and the Sumatra shore [*Singh et al*., 2011]. Despite having traveled 160 km in subduction, this seamount appears intact, unlike the Daiichi-Kashima seamount subducting in the Japan Trench which has been cut by normal faults when entering the trench [*Mogi and Nishizawa*, 1980]. Indeed the Enggano seamount eroded the accretionary prism, creating a depression in the seafloor and being possibly at the origin of a segment boundary in the subduction zone [*Singh et al*., 2011]. Many seamounts have been mapped in the Wharton Basin, including the emerging Cocos-Keeling and Christmas islands and the so-called Christmas Island Seamount Province [*Hoernle et al*., 2011]. Most of these seamounts align along an east-west direction between 10°S and 15°S., and their age is decreasing from 136 Ma to the east to 47 Ma to the west, with anomalously younger ages—44 to 4 Ma—in Christmas Island [*Hoernle et al*., 2011]. It is possible that similar seamounts belonging to the same province existed further north and subducted all along the Sunda Trench from southern Sumatra to Java and eastward. Such seamounts may have let topographic scars and be responsible for subduction erosion and seismic segmentation, as observed in other areas [e.g., *von Huene et al*., 2000; *Singh et al*., 2011]. Conversely, the Roo Rise, a larger plateau located south of Eastern Java, may have more difficulty to enter the subduction, as suggested by the geometry of the Sunda Trench in this area, diverting from the regular arc by a maximum of 60 km [*Kopp et al*., 2006; Figure 11].

6. Conclusions

[58] Our detailed investigations on the Wharton Basin and their consequences on the subduction processes at the Sunda Trench lead us to the following conclusions:

[59] 1. We propose a new, more detailed tectonic map of the Wharton Basin based on the reinterpretation of satellite-derived gravity maps and marine magnetic anomaly profiles. We use the analytic signal method for an objective picking of the magnetic isochrons.

[60] 2. We apply two-plate and three-plate reconstructions (the latter involving the Antarctic plate as well) to better constrain the relative motion between India and Australia from 84 to 38 Ma. The resulting finite rotation parameters, flow lines, and spreading rates represent the best achievable description of this plate motion, despite identified sources of error such as the presence of the diffuse plate

boundary separating the India, Capricorn, and Australia plates since ~20 Ma.

[61] 3. Our model predicts a total compression of ~180 km across the diffuse plate boundary in the Wharton Basin.

[62] 4. Our model predicts that seafloor spreading ceased at ~36.5 Ma (Chron 17y) at the Wharton spreading center.

[63] 5. We use the plate reconstructions to model the structure and age of the subducted slab that we drape on a tomographic model. The close, long-offset fracture zones subducted beneath the Andaman Sea may create zones of weakness, favoring the subducted lithosphere to fold and/or break at large scale.

[64] 6. The compartments of the Wharton Basin located west of the Investigator Fracture Zone entered subduction after spreading cessation at the Wharton spreading center. Conversely, those located east of the Investigator Fracture Zone entered subduction before spreading ceased, leading to the creation of an asthenospheric window, which possibly played a role in the early opening of the South China Sea.

[65] 7. The age of the subducting lithosphere is related to its thickness and buoyancy, resulting in the notion of "subductability" expressed as the extra weight applied on the asthenosphere by the part of the bulk lithospheric density exceeding the asthenospheric density. The Sunda Trench morphology agrees well with these observations, with deep trenches and no fore-arc islands in case of higher subductability off southernmost Sumatra, Java, and eastward, and shallower trench and presence of fore-arc islands in areas of lower subductability off Sumatra and Nicobar islands.

[66] 8. A major deviation from the regular arc which represents the general shape of the Sunda Trench is observed near Sumatra: the trench is progressively displacing inward between compartments B and G, to a maximum of 300 km. This displacement results from the resistance of the younger, warmer, and therefore more buoyant oceanic lithosphere of compartments C–F to the subduction. This lithosphere behaves as an indenter and pushes the accretionary prism forth and up, creating the Sumatran fore-arc islands.

[67] 9. The presence of lithosphere created at slow spreading rate—involving a discontinuous magmatic crust and serpentinized upper mantle rocks—entering subduction in compartment G may weaken the friction on the subduction plan and facilitate the restoration of the accretionary prism above compartment G, resulting in the present geometry.

[68] 10. Local features, including fracture zones and seamounts, may have an effect on the seismic segmentation of the subduction zone. The Roo Rise, a larger volcanic feature, may have more difficulty to enter the subduction and creates a deviation of ~60 km in the trench geometry.

[69] **Acknowledgments.** We are very thankful to the Indo-French Centre for the Promotion of Advanced Research (IFCPAR) for their support in the early part of this study. We also acknowledge the French-Australian Science and Technology (FAST) program for offering the opportunity to collaborate with colleagues at the University of Sydney. VY is grateful to Director, CSIR-National Institute of Oceanography (CSIR-NIO), Goa for permission to publish this paper. We thank G. C. Bhattacharya and P. Patriat for their continuous scientific support. Exchange of data and information with S. C. Cande, N. Chamot-Rooke, C. Deplus, K. S. Krishna, R. D. Müller, S. Singh, and J. M. Whittaker are kindly acknowledged. All figures were drafted with GMT software [*Wessel and Smith*, 1995]. Reviews by Udo Barckhausen, Sang-Mook Lee, and an anonymous reviewer have helped to improve the original manuscript and are kindly acknowledged. This is IPGP contribution number 3481 and NIO contribution number 5512.

References

Barckhausen, U., and H. A. Roeser (2004), Seafloor spreading anomalies in the South China Sea revisited, in *Continent-Ocean Interactions Within East Asian Marginal Seas, AGU Geophysical Monograph (149)*, edited by P. Clift et al., pp. 121–125, AGU, Washington, D. C.

Bourgois, J., and F. Michaud (2002), Comparison between the Chile and Mexico triple junction areas substantiates slab window development beneath north western Mexico during the past 12–10 Myr, *Earth Planet. Sci. Lett.*, *201*, 35–44.

Briais, A., P. Patriat, and P. Tapponnier (1993), Updated interpretation of magnetic anomalies and seafloor spreading stages in the South China Sea: Implications for the Tertiary tectonics of Southeast Asia, *J. Geophys. Res.*, *98*, 6299–6328.

Bullard, E., J. E. Everett, and A. G. Smith (1965), The fit of the continents around the Atlantic, in *A Symposium on Continental Drift, Philos. Trans. (1088)*, edited by P. M. S. Blackett, E. Bullard, and S. K. Runcorn, pp. 41–51, Royal Society, London, U. K.

Cande, S. C. (1976), A paleomagnetic pole from Late Cretaceous marine magnetic anomalies in the Pacific, *Geophys. J. R. Astron. Soc.*, *44*, 547–566.

Cande, S. C., and D. V. Kent (1992), Ultrahigh resolution marine magnetic anomaly profiles: A record of continuous paleointensity variations?, *J. Geophys. Res.*, *97*, 15,075–15,083.

Cande, S. C., and D. V. Kent (1995), Revised calibration of the geomagnetic polarity timescale for the Late Cretaceous and Cenozoic, *J. Geophys. Res.*, *100*, 6093–6095.

Cande, S. C., P. Patriat, and J. Dyment (2010), Motion between the Indian, Antarctica and Africa plates in the early Cenozoic, *Geophys. J. Int*, *183*, 127–149.

Cannat, M. (1993), Emplacement of mantle Rock in the sea floor at mid-ocean ridges, *J. Geophys. Res.*, *98*, 4163–4172.

Cannat, M., D. Sauter, and V. Mendel (2006), Modes of seafloor generation at a melt-poor ultraslow-spreading ridge, *Geology*, *34*, 605–608.

Carlson, R. L., and C. N. Herrick (1990), Densities and porosities in the oceanic crust and their variations with depth and age, *J. Geophys. Res.*, *95*, 9153–9170.

Chaubey, A. K., J. Dyment, G. C. Bhattacharya, J.-Y. Royer, K. Srinivas, and V. Yatheesh (2002), Paleogene magnetic isochrons and palaeopropagators in the Arabian and Eastern Somali basins, NW Indian Ocean, in *The Tectonic and Climatic Evolution of the Arabian Sea Region, Special Publication (195)*, edited by P. D. Clift et al., pp. 71–85, Geological Society, London, U. K.

Chen, Y., and W. J. Morgan (1990), Rift valley / no rift valley transition at mid-ocean ridges, *J. Geophys. Res.*, *95*, 17,571–17,581.

Curray, J. R., F. J. Emmel, D. G. Moore, and R. W. Raitt (1982), Structure, tectonics and geological history of the Northeastern Indian Ocean, in *The Ocean Basins and Margins (6)*, edited by A. E. Nairn and F. G. Stehli, pp. 399–450, Plenum, New York.

Delescluse, M., N. Chamot-Rooke, R. Cattin, L. Fleitout, O. Trubienko, and C. Vigny (2012), April 2012 intra-oceanic seismicity off Sumatra boosted by the Banda-Aceh megathrust, *Nature*, *490*, 240–244.

Demets, C., R. G. Gordon, and J.-Y. Royer (2005), Motion between the Indian, Capricorn and Somalian plates since 20 Ma: Implications for the timing and magnitude of distributed lithospheric deformation in the equatorial Indian ocean, *Geophys. J. Int.*, *161*, 445–458.

Deplus, C., M. Diament, H. Hebert, G. Bertrand, S. Domingues, J. Dubois, J. Malod, P. Patriat, B. Pontoise, and J.-J. Sibilla (1998), Direct evidence of active deformation in the eastern Indian Ocean plate, *Geology*, *26*, 131–134.

Doin, M., and L. Fleitout (1996), Thermal evolution of the oceanic lithosphere: An alternative view, *Earth Planet. Sci. Lett.*, *142*, 121–136.

Dyment, J. (1998), Evolution of the Carlsberg Ridge between 60 and 45 Ma: Ridge propagation, spreading asymmetry, and the Deccan-Reunion hotspot, *J. Geophys. Res.*, *103*, 24,067–24,084.

Dyment, J., and J. Arkani-Hamed (1995), Spreading-rate-dependent magnetization of the oceanic lithosphere inferred from the anomalous skewness of marine magnetic anomalies, *Geophys. J. Int.*, *121*, 789–804.

Dyment, J., S. C. Cande, and J. Arkani-Hamed (1994), Skewness of marine magnetic anomalies created between 85 and 40 Ma in the Indian Ocean, *J. Geophys. Res.*, *99*, 121–124.

Fedorov, P. I., and A. V. Koloskov (2005), Cenozoic volcanism of Southeast Asia, *Petrology*, *13*, 352–380.

Franke, D., M. Schnabel, S. Ladage, D. R. Tappin, S. Neben, Y. S. Djajadihardja, C. Muller, H. Kopp, and C. Gaedicke (2008), The great Sumatra-Andaman earthquakes—Imaging the boundary between the ruptures of the great 2004 and 2005 earthquakes, *Earth Planet. Sci. Lett.*, *269*, 118–130.

Gaina, C., R. D. Muller, B. Brown, T. Ishihara, and S. Ivanov (2007), Breakup and early seafloor spreading between India and Antarctica, *Geophys. J. Int.*, *170*, 151–170.

Gente, P., R. A. Pockalny, C. Durand, C. Deplus, M. Maia, G. Ceuleneer, C. Mevel, M. Cannat, and C. Laverne (1995), Characteristics and evolution of the segmentation of the Mid-Atlantic Ridge between 20 N and 24 N during the last 10 million years, *Earth Planet. Sci. Lett.*, *129*, 55–71.

Gibbons, A. D., U. Barckhausen, P. van den Bogaard, K. Hoernle, R. Werner, J. M. Whittaker, and R. D. Muller (2012), Constraining the Jurassic extend of Greater India: Tectonic evolution of the West Australian margin, *Geochem. Geophys. Geosyst.*, *13*, Q05W13, doi:10.1029/2011GC003919.

Goutorbe, B. (2010), Combining seismically derived temperature with heat flow and bathymetry to constrain the thermal structure of oceanic lithosphere, *Earth Planet. Sci. Lett.*, *295*, 390–400.

Gradstein, F. M., J. G. Ogg, and A. G. Smith (2004), *A Geologic Time Scale*, pp. 500, Cambridge Univ. Press, Cambridge, U. K.

Graindorge, D., et al. (2008), Impact of the lower plate on upper plate deformation at the NW Sumatran convergent margin from seafloor morphology, *Earth Planet. Sci. Lett.*, *275*, 201–210, doi:10.1016/j.epsl.2008.04.053.

Hasterok, D. (2013), A heat flow based cooling model for tectonic plates, *Earth Planet. Sci. Lett.*, *361*, 34–43.

Hebert, H. (1998), Etudes géophysiques d'une dorsale naissante (dorsale d'Aden à l'Ouest de 46°E) et d'une dorsale fossile (dorsale de Wharton): Implications sur les processus de l'accrétion océanique, et à la déformation intraplaque de l'océan Indien [in French], PhD thesis, 372 pp., Univ. Paris, Paris, France.

Hebert, H., B. Villemant, C. Deplus, and M. Diament (1999), Contrasting geophysical and geochemical signatures of a volcano at the axis of the Wharton fossil ridge (N-E Indian Ocean), *Geophys. Res. Lett.*, *26*, 1053–1056.

Hellinger, S. J. (1981), The uncertainties of finite rotations in plate tectonics, *J. Geophys. Res.*, *86*, 9312–9318.

Hoernle, K., F. Hauff, R. Werner, P. van den Bogaard, A. D. Gibbons, S. Conrad, and R. D. Müller (2011), Origin of Indian Ocean Seamount Province by shallow recycling of continental lithosphere, *Nat. Geosci.*, *4*, 883–887, doi:10.1038/ngeo1331.

International Association of Geomagnetism and Aeronomy, Working Group V-MOD (2010), International Geomagnetic Reference Field: The eleventh generation, *Geophys. J. Int.*, *183*, 1216–1230, doi:10.1111/j.1365-246X.2010.04804.x.

Johnson, B. D., C. M. Powell, and J. J. Veevers (1976), Spreading history of the eastern Indian Ocean and greater India's northward flight from Antarctica and Australia, *Geol. Soc. Am. Bull.*, *87*, 1560–1566.

Kirkwood, B. H., J.-Y. Royer, T. Chang, and R. G. Gordon (1999), Statistical tools for estimating and combining finite rotations and their uncertainties, *Geophys. J. Int*, *137*, 408–428.

Klingelhoefer, F., M. A. Gutscher, S. Ladage, J. X. Dessa, D. Graindorge, D. Franke, C. H. André, T. Y. Permana, and A. Chauhan (2010), Limits of the seismogenic zone in the epicentral region of the 26 December 2004 great Sumatra–Andaman earthquake: Results from seismic refraction and wide-angle reflection surveys and thermal modeling, *J. Geophys. Res.*, *115*, B01304, doi:10.1029/2009JB006569.

Kopp, H., E. R. Flueh, C. J. Petersen, W. Weinrebe, A. Wittwer, and M. Scientists (2006), The Java margin revisited: Evidence for subduction erosion off Java, *Earth Planet. Sci. Lett.*, *242*, 130–142.

Kopp, H., et al. (2008), Lower slope morphology of the Sumatra trench system, *Basin Res.*, *20*, 519–529, doi:10.1111/j.1365-2117.2008.00381.x.

Korenaga, T., and J. Korenaga (2008), Subsidence of normal oceanic lithosphere, apparent thermal expansivity, and seafloor flattening, *Earth Planet. Sci. Lett.*, *268*, 41–51.

Krishna, K. S., D. Gopala Rao, M. V. Ramana, V. Subrahmanyam, K. V. L. N. S. Sarma, A. I. Pilipenko, V. S. Scherbakov, and I. V. Radhakrishna Murthy (1995), Tectonic model for the evolution of oceanic crust in the northeastern Indian Ocean from the late Cretaceous to the early Tertiary, *J. Geophys. Res.*, *100*, 20,011–20,024.

Krishna, K. S., J. M. Bull, and R. A. Scrutton (2009), Early (pre-8 Ma) fault activity and temporal strain accumulation in the central Indian Ocean, *Geology*, *37*, 227–230.

Ladage, S., C. Gaedicke, U. Barckhausen, I. Heyde, W. Weinrebe, E. R. Flueh, A. Krabbenhoeft, H. Kopp, S. Fajar, and Y. Djajadihardja (2006), Bathymetric survey images structure off Sumatra, *Eos Trans. AGU*, *87*(17), 165, doi:10.1029/2006EO170001.

Laske, G., and G. Masters (1997), A global digital Map of sediment thickness, *EOS Trans. Am. Geophys. Union*, *78*, Fall Meet. Suppl., F483 (Abstract).

Liu, C. S., J. R. Curray, and J. M. McDonald (1983), New constraints on the tectonic evolution of eastern Indian Ocean, *Earth Planet. Sci. Lett.*, *65*, 331–342.

Macdonald, K. C. (1982), Mid-ocean ridges: Fine scale tectonic, volcanic and hydrothermal processes within the plate boundary zone, *Annu. Rev. Earth Planet. Sci.*, *10*, 155–190.

McKenzie, D. P., and J. G. Sclater (1971), The evolution of the Indian Ocean since the Late Cretaceous, *Geophys. J. R. Astron. Soc.*, *25*, 437–528.

Meng, L., J. P. Ampuero, J. Stock, Z. Duputel, Y. Luo, and V. C. Tsai (2012), Earthquake in a maze: Compressional rupture branching during the 2012 Mw 8.6 Sumatra earthquake, *Science*, *337*, 724–726.

Mihut, D., and R. D. Müller (1998), Revised seafloor spreading history of the Argo Abyssal Plain, in *The Sedimentary Basins of Western Australia 2*, edited by P. G. Purcell and R. R. Purcell, pp. 73–80, Petroleum Exploration Society of Australia, Perth, Australia.

Mogi, A., and K. Nishizawa (1980), Breakdown of a seamount on the slope of the Japan trench, *Proc. Jpn. Acads.*, *56*, 257–259.

Nabighian, M. N. (1972), The analytic signal of two-dimensional magnetic bodies with polygonal cross-section: Its properties and use for automated anomaly interpretation, *Geophysics*, *37*(3), 507–517.

Nabighian, M. N. (1974), Additional comments on the analytic signal of two-dimensional magnetic bodies with polygonal cross section, *Geophysics*, *39*(1), 85–92.

Parsons, B., and J. G. Sclater (1977), An analysis of the variation of ocean floor bathymetry and heat flow with age, *J. Geophys. Res.*, *82*, 803–827.

Patriat, P. (1987), *Reconstitution de l'Évolution du Système de Dorsales de l'océan Indien par les Méthodes de la Cinématique des Plaques*, pp. 308, Terres Australes et Antarctiques Françaises, Paris, France.

Patriat, P., and J. Achache (1984), India-Eurasia collision chronology has implications for crustal shortening and driving mechanism of plates, *Nature*, *311*, 615–621.

Pesicek, J. D., C. H. Thurber, S. Widiyantoro, H. Zhang, H. R. DeShon, and E. R. Engdahl (2010), Sharpening the tomographic image of the subducting slab below Sumatra, the Andaman Islands and Burma, *Geophys. J. Int.*, *182*, 433–453.

Ramana, M. V., T. Ramprasad, and M. Desa (2001), Seafloor spreading magnetic anomlies in the Enderby Basin, East Antarctica, *Earth Planet. Sci. Lett.*, *191*, 241–255.

Roest, W. R., J. Arkani-Hamed, and J. Verhoef (1992), The seafloor spreading rate dependence of the anomalous skewness of marine magnetic anomalies, *Geophys. J. Int.*, *109*, 653–659.

Royer, J.-Y., and R. G. Gordon (1997), The motion and boundary between the Capricorn and Australian plates, *Science*, *277*, 1268–1274.

Royer, J.-Y., and D. T. Sandwell (1989), Evolution of the eastern Indian Ocean Since the Late Cretaceous: Constraints from GEOSAT altimetry, *J. Geophys. Res.*, *94*, 13,755–13,782.

Royer, J. Y., J. W. Peirce, and J. K. Weissel (1991), Tectonic constrains on the hot-spot formation of Ninetyeast Ridge, in *Proc. ODP, Sci. Results*, vol. 121, edited by J. K. Weissel et al., pp. 763–776, Ocean Drilling Program, College Station, Tex.

Ruff, L., and H. Kanamori (1980), Seismicity and the subduction process, *Phys. Earth Planet. Inter.*, *23*, 240–252.

Sager, W. W., L. G. Fullerton, R. T. Buffler, and D. W. Handschumacher (1992), Argo Abyssal Plain magnetic lineations revisited: Implications for the onset of seafloor spreading and tectonic evolution of the eastern Indian Ocean, in *Proc. ODP, Sci. Results*, vol. 123, edited by F. M. Gradstein et al., pp. 659–669, Ocean Drilling Program, College Station, Tex.

Samuel, M. A., N. A. Harbury, A. Bakri, F. T. Banner, and L. Hartono (1997), A new stratigraphy for the islands of the Sumatran Forearc, Indonesia, *J. Asian Earth Sci.*, *15*(4–5), 339–380.

Sandwell, D. T., and W. H. F. Smith (2009), Global marine gravity from retracked Geosat and ERS-1 altimetry: ridge Segmentation versus spreading rate, *J. Geophys. Res.*, *114*, B01411, doi:10.1029/2008JB006008.

Satriano, C., E. Kiraly, P. Bernard, and J.-P. Vilotte (2012), The 2012 Mw 8.6 Sumatra earthquake: Evidence of westward sequential seismic ruptures associated to the reactivation of a N-S ocean fabric, *Geophys. Res. Lett.*, *39*, L15302, doi:10.1029/2012GL052387.

Schlich, R. (1975), Structure et âge de l'océan Indien occidental, *Mem. Hors Service Soc. Geol. France*, *6*, pp. 103.

Schlich, R. (1982), The Indian Ocean: Aseismic ridges, spreading centers and ocean basins, in *The Ocean Basins and Margins (6)*, edited by A. E. Nairn and F. G. Stehli, pp. 51–147, Plenum, New York.

Schouten, H., and K. McCamy (1972), Filtering marine magnetic anomalies, *J. Geophys. Res.*, *77*, 7089–7099.

Sclater, J. G., and R. L. Fisher (1974), Evolution of the east central Indian Ocean, with emphasis on the tectonic setting of Ninetyeast Ridge, *Geol. Soc. Am. Bull.*, *85*, 683–702.

Sclater, J. G., M. Munschy, R. L. Fisher, P. Weatherall, S. C. Cande, P. Patriat, H. Bergh, and R. Schlich (1997), *Geophysical Synthesis of the Indian/Southern Oceans: Part 1, The Southwest Indian Ocean, SIO Reference Series (97–6)*, University of California, San Diego, Calif.

Shulgin, A., H. Kopp, D. Klaeschen, C. Papenberg, F. Tilmann, E. R. Flueh, D. Franke, U. Barckhausen, A. Krabbenhoeft, and Y. Djajadihardja (2013), Subduction system variability across the segment boundary of the 2004/2005 Sumatra megathrust earthquakes, *Earth Planet. Sci. Lett.*, *365*, 108–119, doi:10.1016/j.epsl.2012.12.032.

Singh, S. C., et al. (2008), Seismic evidence for broken oceanic crust in the 2004 Sumatra earthquake epicentral region, *Nat. Geosci.*, *1*, 777–781, doi:10.1038/ngeo336.

Singh, S. C., H. Carton, A. S. Chauhan, S. Androvandi, A. Davaille, J. Dyment, M. Cannat, and N. D. Hananto (2010), Extremely thin crust in the Indian Ocean possibly resulting from Plume-Ridge Interaction, *Geophys. J. Int.*, *184*, 29–42, doi:10.1111/j.1365-246X.2010.04823.x.

Singh, S. C., et al. (2011), Aseismic zone and earthquake segmentation associated with a deep subducted seamount in Sumatra, *Nat. Geosci.*, *4*, 308–311, doi:10.1038/ngeo1119.

Singh, S. C., A. P. S. Chauhan, A. J. Calvert, N. D. Hananto, D. Ghosal, A. Rai, and H. Carton (2012), Seismic evidence of bending and unbending of subducting oceanic crust and the presence of mantle megathrust in the 2004 Great Sumatra earthquake rupture zone, *Earth Planet. Sci. Lett.*, *321–322*, 166–176, doi:10.1016/j.epsl.2012.01.012.

Smith, W. H. F., and D. T. Sandwell (1997), Global seafloor topography from satellite altimetry and ship depth soundings, *Science*, *277*, 1956–1962.

Stein, C., and S. Stein (1992), A model for the global variation in oceanic depth and heat flow with lithospheric age, *Nature*, *359*, 123–129.

Stern, R. J. (2002), Subduction zones, *Rev. of Geophys.*, *40*, 1012, doi:10.1029/2001RG000108.

Tikku, A. A., and S. C. Cande (1999), The oldest magnetic anomalies in the Australian-Antarctica Basin: Are they isochrons?, *J. Geophys. Res.*, *104*, 661–677.

Tikku, A. A., and S. C. Cande (2000), On the fit of Broken Ridge and Kerguelen Plateau, *Earth Planet. Sci. Lett.*, *180*, 117–132.

Turcotte, D. L., and G. Schubert (1982), *Geodynamics: Applications of Continuum Physics to Geological Problems*, John Wiley and Sons, New York.

von Huene, R., C. R. Ranero, and W. Weinrebe (2000), Quaternary convergent margin tectonics of Costa Rica, segmentation of the Cocos Plate, and Central American volcanism, *Tectonics*, *19*, 314–334.

Wessel, P., and W. H. F. Smith (1995), New version of the Generic Mapping Tools released, *Eos Trans. AGU*, *76*, 329.

White, R. S., D. P. McKenzie, and R. O'Nions (1992), Oceanic crustal thickness from seismic measurements and rare earth elements inversions, *J. Geophys. Res.*, *97*, 19, 683–19,715.

Whittaker, J. M., R. D. Muller, G. Leitchenkov, H. Stagg, M. Sdrolias, C. Gaina, and A. Goncharov (2007a), Major Australian-Antarctic plate reorganization at Hawaiian-Emperor bend time, *Science*, *318*, 83–86.

Whittaker, J. M., R. D. Muller, M. Sdrolias, and C. Heine (2007b), Sunda-Java trench kinematics, slab window formation and overriding plate deformation since the Cretaceous, *Earth Planet. Sci. Lett.*, *255*, 445–457.

Yatheesh, V., et al. (2008), Central Indian Ocean plate tectonics between Chrons 34 to 20 (83 to 42 Ma) revisited, *EOS Trans. Am. Geophys. Union*, *89*(53), Fall Meet. Suppl. (Abstract).

Yue, H., T. Lay, and K. D. Koer (2012), The great intraplate earthquakes of 11 April 2012: En echelon and conjugate fault ruptures on an emerging Indian-Australian plate boundary, *Nature*, *490*, 245–249.